UC Irvine
UC Irvine Electronic Theses and Dissertations

Title
Structure-Process-Property Relationships for LENS® and SLM Processed AlSi10Mg Alloys and the Effect of Heat Treatment

Permalink
https://escholarship.org/uc/item/8s14j0sn

Author
Ramesh, Nithya

Publication Date
2018

Supplemental Material
https://escholarship.org/uc/item/8s14j0sn#supplemental

Peer reviewed|Thesis/dissertation

eScholarship.org Powered by the California Digital Library
University of California

UNIVERSITY OF CALIFORNIA,

IRVINE

Structure-Process-Property Relationships for LENS® and SLM Processed AlSi10Mg Alloys and the Effect of Heat Treatment

THESIS

submitted in partial satisfaction of the requirements

for the degree of

MASTER OF SCIENCE

in Materials Science and Engineering

by

Nithya Ramesh

Thesis Committee:

Professor Julie M. Schoenung, Chair

Provost and Executive Vice Chancellor Enrique J. Lavernia

Assistant Professor Timothy Rupert

2018

© 2018 Nithya Ramesh

DEDICATION

To

my parents, sister and family,

Thank you for the endless motivation and support throughout the two years. I wouldn't have been able to achieve this without all of it.

TABLE OF CONTENTS

LIST OF FIGURES

LIST OF TABLES

ACKNOWLEDGEMENTS

I would like to express my heartfelt gratitude to my committee chair Professor Julie M. Schoenung for thoroughly encouraging me and providing me this opportunity. I am deeply indebted to her for constantly pushing me to achieve my target. I would also like to express my gratitude to my committee members, Provost Enrique Lavernia and Professor Timothy Rupert, whose knowledge and appreciation for engineering and research has been a perpetual source of inspiration throughout the graduation phase of my life. I would like to thank Professor Lianyi Chen from Missouri State University for providing us with the SLM as-deposited sample for the study. I would like to acknowledge my lab family for all their guidance throughout my research and for helping me in my transition to become a graduate student. Their moral support prepared me to face all my trials and tribulations with grit and determination. Lastly, I would like to acknowledge the financial support provided by the NSF-CBET grant #1605392.

ABSTRACT OF THE THESIS

Structure-Process-Property Relationships for LENS® and SLM Processed AlSi10Mg Alloys and the Effect of Heat Treatment

By

Nithya Ramesh

Master of Science in Materials Science and Engineering

University of California, Irvine, 2018

Professor Julie M. Schoenung, Chair

Additive manufacturing has developed as a strong tool in making parts with complex shapes and high qualities. The microstructure evolution of the AlSi10Mg alloy manufactured through Laser Engineered Net Shaping (LENS®) and Selective Laser Melting (SLM) AM techniques is studied through electron microscopy characterization. The solidified melt pools of both as-deposited samples exhibit a "fish scale" pattern that is inherent to the AM process. A very fine cellular microstructure is seen due to the high thermal gradients and cooling rates on the order of 10^3-10^6K/s. Eutectic silicon forms along the cell boundaries of the aluminum matrix. The rapid solidification and non-equilibrium conditions result in the formation of metastable phases. X-Ray Diffraction and Differential Scanning Calorimetry analysis were carried out to identify the phases in the as-deposited samples. In-situ and post-mortem TEM characterization were conducted to observe the formation of silicon and Mg_2Si precipitates. The Mg_2Si precipitates segregated along the cell boundaries in both of the as-deposited samples. The π-$Al_8Si_6Mg_3Fe$ phase was also observed to segregate along the cell

boundary. High resolution transmission electron microscopy studies revealed a crystallographic orientation relationship between the [001] Al matrix and the [110] Si primary phase. A comparative study between the microstructure of the LENS® and SLM as-deposited samples revealed a finer microstructure in the as-deposited SLM sample. A conventional T6 heat treatment caused the cellular network to break down and the Si particles to coarsen. Microhardness tests were conducted on the as-deposited samples and heat-treated samples to correlate the mechanical properties with the microstructure. The hardness of the as-deposited samples was 105 HV which is higher than the hardness of a cast counterpart.

CHAPTER 1

INTRODUCTION

Additive manufacturing (AM) is the process of joining materials layer by layer from a 3D CAD model. It is also known as rapid prototyping, rapid manufacturing, direct digital manufacturing, layer manufacturing or solid freedom fabrication [1]. The process of using layered methods dates to the early 1890s [2]. The AM emerged in the 1950s and has advanced over the years as a tool for prototyping to being used for developing end use products. It is used in the aerospace, automobile and medical industries through material development and process optimization. The AM technology consists of the following three steps:

[a] Creation of a CAD 3D file based on the design geometry.

[b] Slicing of the 3D part into stacks of 2D layers and converting to a .stl file or a standard AM format that is readable by the machine.

[c] Printing of the part through the simultaneous interaction of energy source and feedstock.

Compared to other subtractive manufacturing processes, AM offers potential advantages such as designing parts with complex geometries that cannot be built with conventional subtractive processes; eliminating tooling requirements, fixtures and other auxiliaries such as coolants and fluids; minimizing material waste; environmental friendly and cost effective for prototyping and small batches [3].

Several AM techniques have been developed in the past years. ASTM classifies these techniques into seven categories: Stereolithography, Material Jetting, Binder Jetting, Material Extrusion, Powder Bed Fusion, Sheet Lamination, and Directed Energy Deposition [4]. They can further be classified based on the feedstock used or on the energy source. The materials that can be used are metals, polymers, ceramics and composites. The usual energy sources used are plasma, laser or electron beam to irradiate the feedstock.

Metal AM can be classified as follows as seen in ***Figure 1*** [5]:

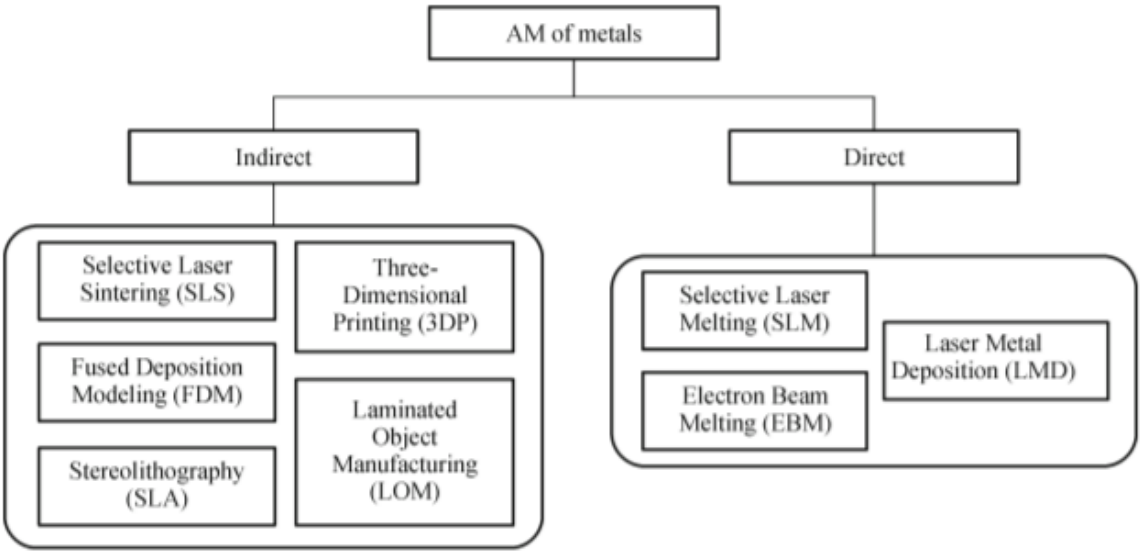

Figure 1 Classification of metal AM [5]

In the indirect methods a binder is used to bond the metal particles and in the direct methods the metal particles are melted through an energy source. In our study, AlSi10Mg manufactured through the Laser Engineered Net Shaping (LENS®) and Selective Laser Melting (SLM) techniques is studied.

1.1 Laser Engineered Net Shaping (LENS®) and Selective Laser Melting (SLM):

The LENS® technology is a part of the Directed Energy Deposition (DED) class and was originally developed at Sandia National Laboratories in collaboration with Pratt & Whitney and then licensed to Optomec Inc. in 1997 [3]. It is capable of manufacturing near net shaped metallic components with nearly full density. A schematic description of the LENS® process is shown in ***Figure 2***.

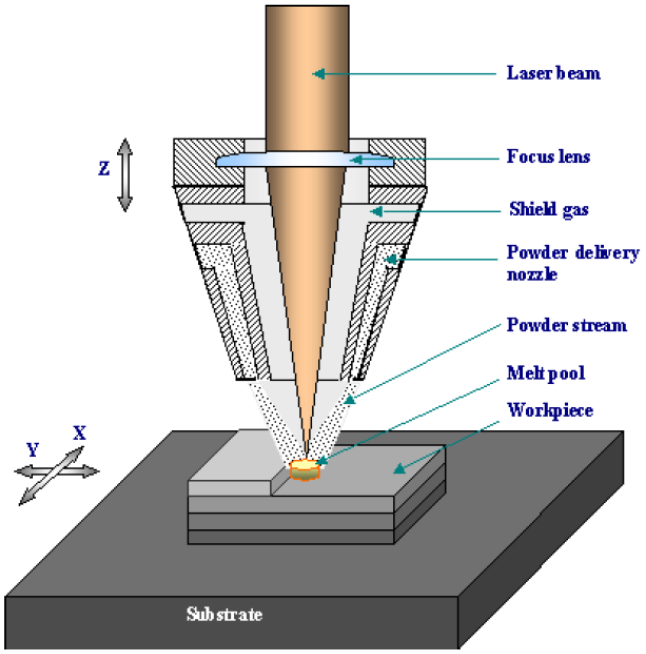

Figure 2 Schematic description of the LENS process

This consists of a high powered laser, usually CO_2 or Nd:YAG fiber lasers, that focuses on the substrate creating a melt pool. The powder feedstock is fed into an external powder hopper and is carried to the chamber through argon carrier gas and is deposited through the nozzles on to the melt pool [6]. The stage onto which the substrate is attached can move along the X-Y direction and the laser beam is incremented in the Z direction. The movement of the stage and the laser is controlled by the CAD input file. The layers are metallurgically bonded. A

high cooling rate on the order of 10^3- 10^4 K/s [7] and large thermal gradients are created due to the small melt pool and rapid solidification. This gives the LENS® processed parts a very fine microstructure and superior mechanical properties compared to the conventional processes. A variety of materials such as steels [8], [9], Ni alloys [10], Ti alloys [11] and Al alloys [12], [13], [14] have been researched and successfully deposited through the AM process. Functionally graded materials can be deposited by gradually changing the composition one layer at a time. The microstructure and properties of each material can be controlled through optimizing the laser parameters such as laser scan speed, power, hatch rotation and scan spacing [15]. A brief discussion on how the process parameters affect the properties is presented in the section below.

Selective Laser Melting (SLM)

Selective Laser Melting is a powder bed fusion process in which a layer of powder is spread across the substrate. The laser beam rasters the powder bed and melts selected areas of the powder bed based on the input CAD file. Upon completion of a layer, the powder build platform moves downward along the Z direction and another layer of powder is spread through the recoater. A schematic description of the SLM process is shown in ***Figure 3*** [16].

The rapid solidification rate produces high cooling rates of the order 10^3-10^6 K/s in SLM [17]. The SLM parts also show excellent mechanical properties and corrosion resistance compared to cast counterparts. Many materials including stainless steels, tool steels, nickel alloys, cobalt alloys and aluminum alloys have been processed successfully using SLM [15].

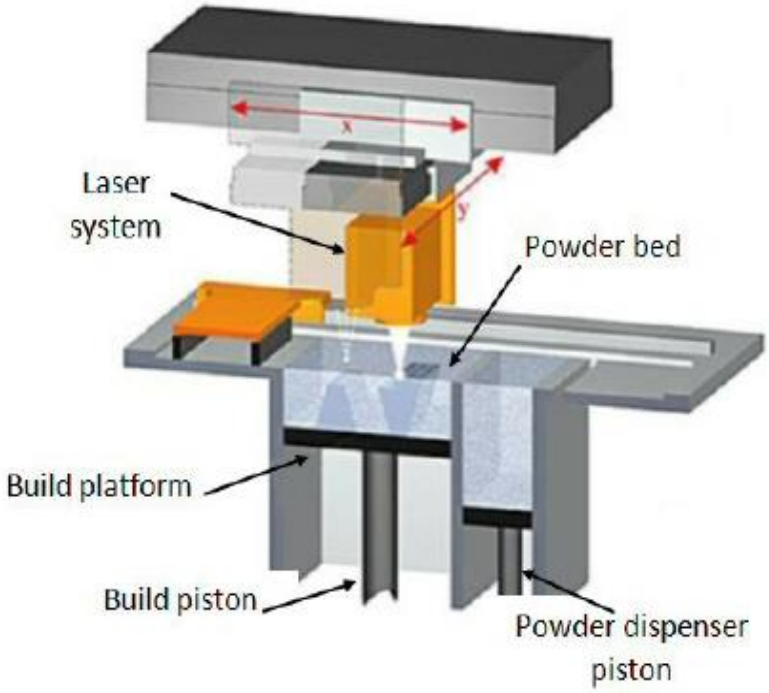

Figure 3 Schematic description of the SLM process [16]

The mechanical properties are controlled by the microstructure. It is well known that grain refinement is one of the mechanisms through which the microstructure can be modified to give parts with higher strengths. Grain refinement in Al alloys can be achieved through (i) chemical modification, (ii) severe plastic deformation, or (iii) through a combination of both [18]. However, the formation of complex geometries in one step is still not achievable through the conventional methods. Through the LENS® and SLM process, complex geometries can be built with fine grains and excellent mechanical properties because of the high cooling rates and large thermal gradients. There are some differences between the LENS® and SLM processes that may affect the microstructure of the final product. The LENS® employs higher power density than SLM for the same material composition. A comparative study between the Ni_3Al intermetallic alloy processed through LENS® and SLM

revealed that the SLM-processed materials are finer than the LENS®-processed materials [19]. Attar et al., [20] studied SLM and LENS® processed commercially pure titanium. They reported the formation of mixed plate-like, widmanstatten and serrated morphologies in LENS® samples, while only martensitic α' phase microstructure was observed in SLM samples due to the difference in cooling rates. A higher strength was also reported for the SLM samples compared to the LENS® processed samples. In this work, AlSi10Mg alloy is processed through LENS® and SLM and the microstructural differences and change in phase transitions due to the two processing differences are studied. The Al-Si-Mg alloys are desirable in aerospace and automobile industries due to its light weight and high strength to weight ratio. The processing of these alloys using LENS and SLM have gained wide attention due to the fine microstructure and high hardness. AlSi10Mg components show a wide range of mechanical properties based on solidification parameters [21]

1.2 Effect of processing parameters on the final part

The processing of aluminum alloys presents unique challenges compared to the processing of titanium or stainless steels. [22]. The main challenges with aluminum all is its high reflectivity and high thermal conductivity, which require higher laser power to overcome heat dissipation and poor absorption. The aluminum powder also has poor flowability due to its light weight and low viscosity in molten form. The formation of aluminum oxides increases the presence of porosity [23]. Extensive literature is available on optimizing different processing parameters such as energy density, scanning strategy, hatch rotation to get fully dense parts with minimum porosity for AlSi10Mg alloys processed through SLM [24],[25]. ***Table 1*** compares the different properties of aluminum and other AM candidate

materials [23]

Table 1 Properties of AM candidate materials [23]

Material	**Flowability (s/50 gm)**	**Thermal Conductivity (W/(mK))**	**Reflectivity (%)**
Ti64	47	6.7	53-59
Stainless Steel 316	14.6	21.4	60
Al6061	77	172	91
AlSi10Mg	No flow	146	91

The importance of the Al-Si alloys in automobile and aerospace industries have led to extensive research in the AM of these alloys [26] . The formation of a consolidated part with high density can be achieved through optimization of process parameters and controlling the feedstock characteristics. Abhoulkair et al., summarized the factors controlling the quality of the builds, as shown in ***Figure 4*** [24].

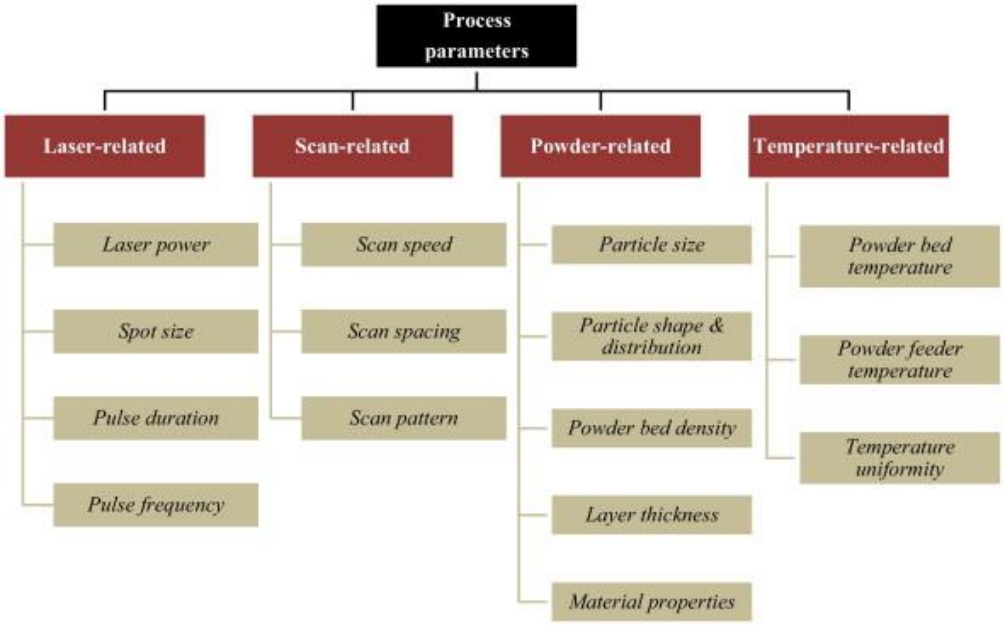

Figure 4 Process parameters controlling final part in AM [24]

1.2.1 Energy Density:

The energy density of the laser is given by

$$\psi = \frac{P}{v * h * t}$$

where P, v, h and t are the laser power, scan speed, hatching distance and layer thickness.

Many studies have been carried out to optimize the energy density during AM. The laser power and scan speed are the most important parameters. E.O Olankami et al., [27] studied single layers of pure Al, Al-Si and Al-Mg powders with different scan speeds and laser power to determine a processing window within which good quality parts with minimum porosity and balling could be deposited. Balling is the formation of balls of material due to improper wetting of the surface because of high surface tension. The processing window was investigated by employing a laser power of between 20 and 240 W, and scanning speeds of between 20 and 250 mm/s, with a constant hatch distance of 0.1 mm. They identified four regions in the process window, namely: no marking, partial marking, good consolidation and excess balling. At low energy densities, agglomeration of powder particles and unmelted powder particles were observed showing insufficient densification resulting in the no marking region. Higher energy densities create keyhole melting, which leads to vaporization of the elements and this region caused balling. Louis et al., [26] studied producing nearly fully dense parts with high scan speeds and a minimum laser power. A minimum laser power of 150 W is required to produce aluminum parts with nearly full density [28]. However, a high laser power creates balling due to unstable melt pools [29].

High scan speeds can cause insufficient melting and bonding of the powder resulting in porosity and poor density of the parts. As the layer thickness is set proportional to the Z height increment in LENS®, this causes an increase in the working distance and ultimately stops deposition [1]. Although lower scan speeds may be ideal, this increases the time taken to build a full part. Scan speed also affects the porosity of the build [24]. Abhoulkair et al., observed two kinds of pores in their study, as shown in . Small spherical pores, referred to as metallurgical pores, are caused by evaporation of trapped gases within the melt pool or from the powder. These occur at lower scan speeds. Irregular shaped, large pores, referred to as keyhole pores, are due to keyhole instability and lack of fusion.

1.2.2 Scan spacing

Abhoulkair et al., [30] studied the effect of different hatch spacings of 50, 100 and 150 µm on AlSi10Mg processed in SLM by keeping laser power and scan speed constant, as shown in ***Figure 5***. At small hatch spacings of 50 and 100 µm, the parts were well consolidated. At higher hatch spacing of 150 µm, porosity occurred. An increase in hatch spacing reduces the overlap from track to track and diminishes the bonding strength.

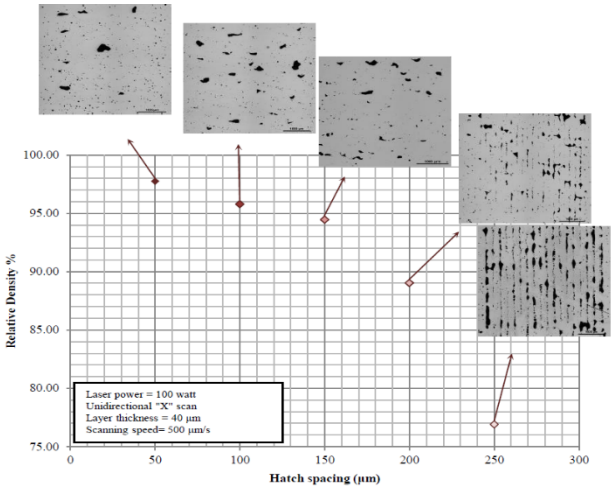

Figure 5 Effect of changing hatch spacing on density

1.2.3 Scanning strategy

Scanning strategy is defined as the geometrical pattern in which the laser rasters across the surface. There are different scanning strategies, as shown in ***Figure 6***. In our study, the LENS® deposited sample was scanned using an alternating hatch rotation of 90^{O} between each layer. The SLM sample was deposited using the unidirectional scanning strategy.

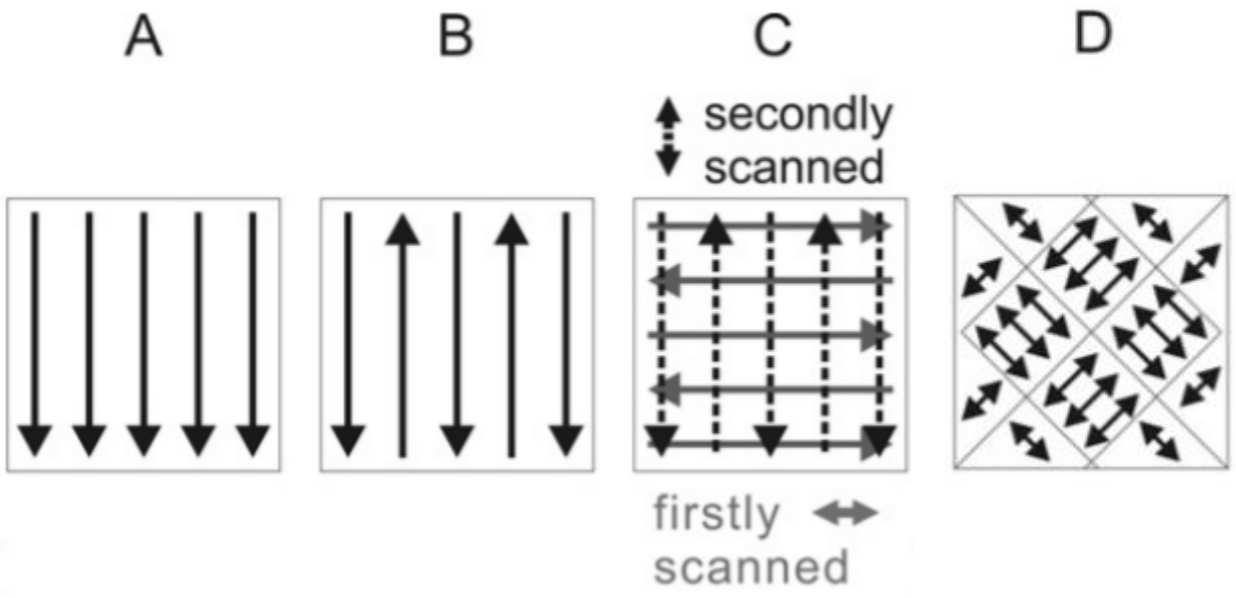

Figure 6 Different scanning strategies (a) Unidirectional (b) Bidirectional (c) Rotation of 90 degrees (d) Island [32]

The scanning strategy has an influence on porosity and distribution of thermal stresses. Carter et al., reported a microstructure change in CM247LC nickel superalloy between the unidirectional and island shift scanning strategy [31]. Thijs et al., [32] reported a controlled texture in the SLM deposited Al-Si-Mg alloys by changing the scanning strategy. A strong <100> texture along the scanning direction was seen when a unidirectional scanning strategy was observed. However, when the scanning direction is rotated by 90^{O} every layer, the texture reduced significantly. A correct scanning strategy can also reduce the residual stress build-up in the sample. Smaller islands were found to have the least residual stress

[33]. Wrapping and distortions due to residual stresses can also be minimized by adopting the right scanning strategy. A 45^{O} rotation was found to have the least residual stress build up, according to results from a finite element (FE) model that was developed to investigate the thermomechanical responses in the SLM process. The maximum stress build-up was found to be with the unidirectional scanning strategy [34].

1.3 Al-Si-Mg alloys

The Al alloys have low density (2.7 g/cm^3), high strength to weight ratio, good weldability and excellent corrosion resistance [35]. As the demand for low fuel consumption and environmentally friendly products increases, the application of Al alloys has increased in the automotivee and aerospace industries. The Al-Si alloys are the most important cast alloys due to their high fluidity and low shrinkage [36]. Mg is added to the Al-Si alloys to improve the strength through the formation of the Mg_2Si precipitation hardening phase. The AlSi10Mg composition used in our work is a near eutectic composition, which reduces the solidification temperature and makes it easier to process.

The aluminum alloys usually manufactured through the conventional routes such as casting, forging and extrusion exhibit coarse grained structures [37]. The casting alloys also have plate-like silicon morphology, which decreases the ductility of the alloy. It is well known that the strength of the material can be modified through grain refinement. The mechanical properties of the alloys also depend on the dendrite arm spacing, the silicon distribution and morphology, and the formation of the Mg_2Si precipitates [38]. A number of studies have been done in casting to modify the morphology of the flake-like eutectic silicon precipitates into fibrous silicon precipitates, which impart good ductility and strength to the alloy. Chemical

modifiers such as Na and Sr are effective in refining the silicon morphology [39]. Modifying the cooling rate is another effective strategy to modify the morphology of silicon. Both the LENS® and SLM processes have high cooling rates because of the rapid solidification, which results in very fine structures with improved strength. The non-equilibrium solidification also results in formation of metastable phases. While the formation of the distinct as-solidified microstructures has been well explained [40], few previous studies have focused on the formation of the Mg_2Si phase and how it is affected by heat treatment.

Numerous studies have been carried out to understand the precipitation sequence and kinetics in Al-Si-Mg alloys and the following sequence has become widely accepted [41].

Si clusters $\longrightarrow$ Si Mg co clusters $\longrightarrow$ GP I zones $\longrightarrow$ β'' $\longrightarrow$ β' $\longrightarrow$ $\beta(Mg_2Si)$

The rapid water quench after the solution treatment creates quenched-in vacancies. This is accompanied by the formation of silicon clusters. The Mg atoms move towards the silicon clusters. The GP zones are few layers of atoms thick. The β'' precipitates, which is the primary hardening phase, are needle shaped. They have monoclinic crystal structure with lattice parameters: a=1.516 nm, b=0.405 nm, c=0.674 nm (β=105.3°). They are coherent with the aluminum matrix and are oriented along the $<001>_{Al.}$ The β' phase is semi-coherent with the matrix and has an hexagonal structure and lattice parameters: a=0.705 nm, c=1.215 nm. The incoherent equilibrium β phase has an antifluorite structure and is incoherent with the matrix and has non-hardening effect.

This work aims to study the microstructural evolution of AlSi10Mg alloys processed through LENS® and draw a comparison between the microstructural evolution in SLM and LENS® processed AlSi10Mg alloys. One of the main objectives of this study is to understand if the

high cooling rates in AM affect the formation of the heat treatable Mg_2Si phase. The effect of heat treatment on the microstructure is studied through in-situ heating and post mortem TEM characterization. The response of the LENS® processed AlSi10Mg alloy to precipitation hardening treatment is studied and compared to the response in cast alloys, through mechanical hardness testing.

CHAPTER 2

EXPERIMENTAL METHODS

In this chapter, a description of all the materials and equipment used for sample fabrication and the characterization, and mechanical test methods employed is provided.

2.1 Production of fully dense parts through AM

Test cubes for study were deposited using the SLM and LENS® AM techniques. The AlSi10Mg powder used in the LENS® system was gas atomized and obtained from Valimet Inc. and had a particle size distribution of 40-100 μm. It was processed through LENS® using the Optomec 750 Laser Engineered Nest Shaping (LENS®) system seen in ***Figure 7***. The AlSi10Mg powder used in SLM was obtained from Honeywell.

A cube of size 1 x 1 x 1.5 cm was deposited, with the LENS® system. The height of the cube was made tall enough to enable microstructural gradient studies across the height of the build. As aluminum is highly reactive compared to titanium and steels, the process was conducted under Argon atmosphere (less than 10 ppm O_2) to prevent any oxidation during the melting of powder. A Nd:YAG laser was used to melt the powder fed from four nozzles. The following process parameters were used based on optimization done from a previous study done in the group.

- Laser Power – 600 W
- Scan Speed – 0.02 m/s
- Layer Thickness – 0.04 cm
- Hatch Spacing – 0.03 cm

A very high laser power of 600 W is required to make nearly fully dense parts due to the high reflectivity of aluminum. An alternating hatch scan strategy with a 90^{O}rotation between layers was used.

Figure 7 Optomec LENS® 750

AlSi10Mg powder was processed through the SLM technique at Dr. Chen's lab at Missouri State University. A cube of size 8.3 mm was deposited, as shown in ***Figure 8***. A laser power of 200 W and a scan speed of 0.46 m/s was used during deposition.

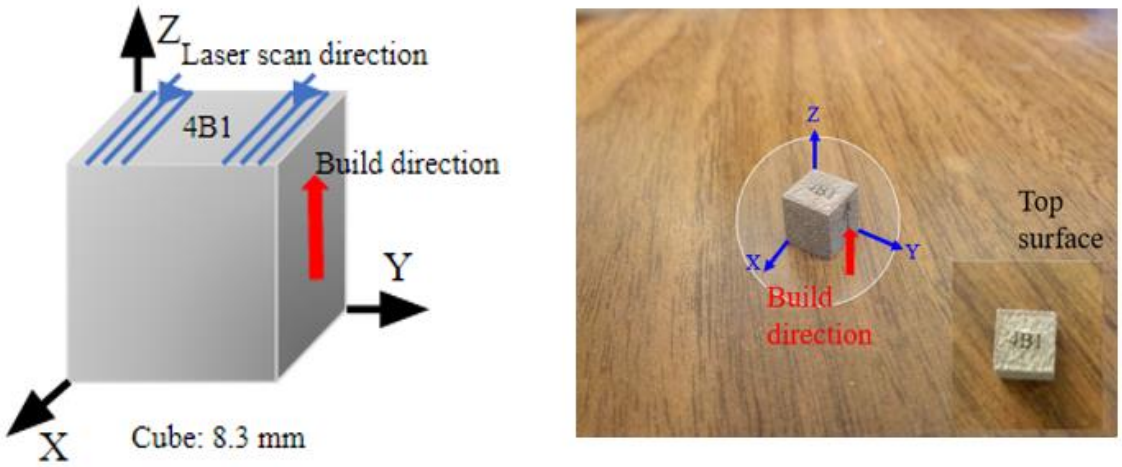

Figure 8 Geometry and scanning pattern of the as-deposited SLM sample

2.2 Phase Identification

The rapid solidification in AM produces a non-equilibrium condition and may form metastable phases. Thermal analysis on the powder and on the LENS® and SLM as-deposited samples was done to identify the precipitation reactions. Differential scanning calorimetry (DSC) analysis was done on the samples in a purified argon atmosphere using a Netschz 404 F3 (NETZSCH Instruments, Burlington, Massachusetts). Aluminum pans were used. The device-specific heat flow should be eliminated from the raw data. An empty aluminum reference pan was used for this to get a baseline measurement. This was then subtracted from the sample measurement. Temperature scans were made from 20 ^{o}C to 500 ^{o}C at a heating rate of 10^{o}C/minute while flowing Ar gas.

A Rigaku Smartlab X-ray diffractometer (Rigaku Analytical Devices, Wilmington, Massachusetts) was used for XRD analysis to identify the phases, utilizing Cu Kα radiation and a scan speed of 2.0 degree/min for the 2θ range from 20°-110°. Bulk samples processed

in the LENS® and SLM were scanned and compared with the diffraction pattern of the powder samples to confirm phase consistency.

2.3 Bulk material characterization

AM alloys have a complex thermal history involving directional heat extraction, and repeated melting and rapid solidification. AM fabricated alloys also experience repeated solid-state phase transformations [42]. Electron microscopy characterization was performed to understand the complex nature of the microstructure formed after processing. For this endeavor, samples were cut parallel and perpendicular to the build direction along the X-Z and X-Y planes, as shown in ***Figure 9***. The samples were cut using a slow diamond wheel saw and care was taken to avoid heating of the sample during cutting.

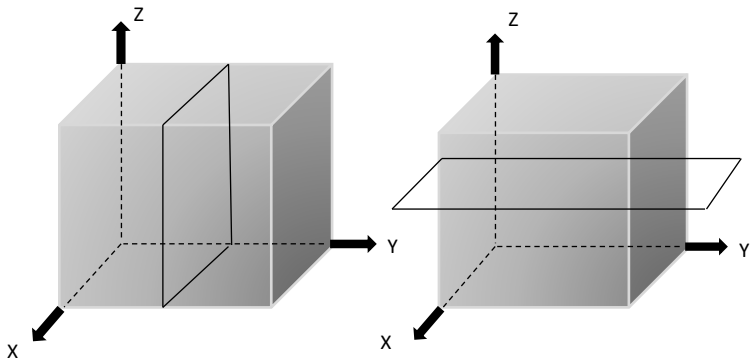

Figure 9 Samples characterized along (a) XZ plane (b) XY plane

2.3.1 SEM Characterization

The test specimens were mounted in KonductoMet conductive filled phenolic mounting compound using a Buehler SimpliMet 1000 Automatic Mounting Press (Buehler, Lake Bluff, Ill.). The samples were polished metallographically to 1 μm diamond suspension using a Buehler EcoMet 250 grinder-polisher. The samples were etched using Kellers reagent

comprising of 3% HF, 10% HNO3, and 87% H2O (vol. %) for 15 s. A FEI Quanta 3D FEG (FEI, Hillsboro, Oregon) dual beam SEM at 15 keV was used to characterize the sample. Energy dispersive X-ray (EDX) analysis was carried out to determine the chemical composition of the build parts. It also helped to determine if the alloying elements present are being lost through evaporation during this high temperature process. INCA™ software was used to analyze the results.

2.3.2 TEM Characterization

The high cooling rates associated with AM produce finer microstructures [43]. As the optical resolution to identify the cells and precipitates was not high enough in the SEM, transmission electron microscopy (TEM) was used to characterize the nano-sized precipitates and determine crystal orientation relationships between the different phases. Samples were cut perpendicular and parallel to the build direction for characterization, as shown previously in ***Figure 9***. A thin foil was prepared by polishing the sample metallographically using 1200 grit size SiC paper in Buehler EcoMet 250 grinder-polisher to a thickness of 50 μm. A 3 mm TEM sample was obtained from the foil by punching. It was further reduced to a thickness of 30 μm through dimpling. The dimpled sample was then ion milled using the PIPS II (Gatan Inc, Pleasanton, California) system to get electron transparent regions, and liquid nitrogen was used to protect the samples from damage during milling. The sample was ion milled at 5.5 keV at an angle of 6^{o} (top gun) and 4^{o} (bottom gun) until a perforation was seen, after which it was milled at 1.7 keV for 20 minutes at an angle of 4^{o} (top gun) and 2^{o} (bottom gun). A one minute clean up at 0.1 kev was used to remove any milling deposits. The JEOL 2800 and 2100F (JEOL USA Inc, Peabody, Massachusetts) transmission electron microscopes

operating at 200 keV were used for characterization. STEM-EDS characterization was done using the JEOL JEM 2800 to see the composition distribution in the sample.

Due to the repeated heating and cooling during AM, partial re-melting of successive layers will occur. Y.J. Liu et al., reported that the cooling rate in the top surface of the melt pool reaches 1.44×10^{6} K/s, which is much higher than that at the bottom $\leq1\times10^{3}$ K/s [37]. This gradient in cooling rate may also cause a gradient in microstructure. To study this gradient in microstructure, samples were cut parallel to the build direction and taken from two different heights: from the top surface and from the surface close to the substrate in the LENS® deposited sample, as shown in ***Figure 10*** TEM characterization was done on the JEOL 2100 and cell sizes were noted for the two samples.

A similar gradient study was done on the SLM deposited sample. Samples were taken from two locations along the build direction, one closer to the top surface and another closer to the substrate, as shown in ***Figure 10***. The microstructure gradient was evaluated using a JEOL 2100 TEM.

Al-Si-Mg series alloys are precipitation hardenable alloys. The high cooling rate and thermal gradients in AM make the precipitation mechanisms complex. It has been shown that different cooling rates can lead to the formation or suppression of phases. In-situ heating on the JEOL 2100 was done on the as-deposited SLM sample to observe changes in microstructure and formation of precipitates. Two SLM deposited samples from the top (hereafter referred to as SLM-320) and bottom (hereafter referred to as SLM- 180) of the build parallel to the build direction were taken. SLM-320 was heated using a Gatan in-situ double tilt holder. It was heated at the rate of 10 ^{o}C/minute up to 320 ^{o}C and cooled

instantaneously. A digital reader was connected to observe the temperature change and images were captured at different temperatures using Gatan Digital Micrograph.

SLM-180 was in-situ heated similarly to SLM-320, as described above. It was heated to 180 ^{o}C at the rate of 10 ^{o}C/minute and then held at 180 ^{o}C for 30 minutes, after which it was again heated to 320 ^{o}C at a heating rate of 10 ^{o}C/minute.

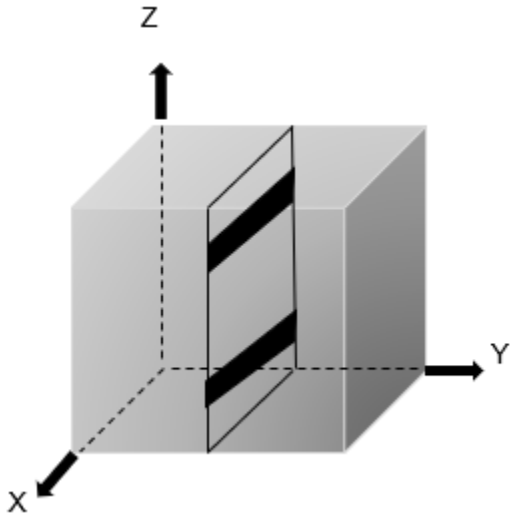

Figure 10 Location of samples for gradient study

2.4 Effect of heat treatment

T. Hu et al., reported that the precipitation behavior in ultra-fine grained aluminum alloys is very different than that in coarse grained aluminum alloys [44]. Ma et.al., performed T6 heat treatment on cryomilled Al7071 alloy and reported that artificial aging at low temperature for a short time period enabled to achieve an equivalent level of strength as can be achieved with the T6 temper [45]. A T6 temper is defined as solution treatment at a higher temperature to form a single phase followed by quenching to obtain a supersaturated solid solution. This is followed by age hardening to cause precipitation from the solid solution [46]. In the current study, a T6 conventional heat treatment was conducted to study the precipitation hardenable Mg_2Si phase. The SLM and LENS® deposited samples were solution

treated in a Cress C601K muffle furnace (Cress, Carson City, Nevada) at 520 ^{o}C for 2 hours and artificially aged at 160 ^{o}C for 12 hours. The effect on microstructure was studied using the JEOL 2800 TEM. STEM-EDS characterization was performed in the JEOL 2800 to see the composition distribution.

Eight samples were cut parallel to the build direction from the as-deposited LENS® samples. Four samples were solutionized at 450 ^{o}C and three of them were artificially aged at 160 ^{o}C for 2, 6 and 12 hours. The other four samples were solutionized at 520 ^{o}C and three of them were artificially aged at 160 ^{o}C for 2, 6 and 12 hours. The Cress furnace was used for these heat treatments. Micrographs of the samples after heat treatment were taken in the SEM to observe the change in morphology.

2.5 Mechanical Properties

AM processed samples have been reported in the literature to have strength values equivalent or greater than heat-treated cast counterparts [47] . Vickers hardness tests on the as deposited sample was carried out in the current study using a Struers Duramin Hardness Tester (Struers, Cleveland, Ohio). A standard Vickers diamond indenter was used for these measurements. A load of 1 kgf was applied for 15 s. The Duramin 5 microindenter software measured the dimensions of the indent diagonals in microns and calculated the hardness according to the following equation:

$$HV = 1 \cdot 854 \frac{F}{D^2}$$

where F is the load in kgf, d is the arithmetic mean of the two diagonals of the indent in mm, and HV is the Vickers hardness. A load of 0.5 kgf was applied for 15 s on the heat treated

samples. As the heat treated samples showed material softening, a smaller load compared to the as-deposited samples had to be applied to measure the diagonals of the indent.

CHAPTER 3

RESULTS & DISCUSSION

3.1 Powder Characterization

3.1.1 Chemical composition

The powder used for the LENS® deposited sample is gas atomized and supplied by Valimet Inc. with the following composition provided by the vendor.

Table 2 Composition of the AlSi10Mg powder as provided by supplier (units of weight percent)

%Al	%Si	%Mg	%Fe	%Mn	%Cu	%Ti	%Zn
Bal.	10.00	0.39	0.15	0.04	<0.01	0.01	0.01

The high temperature in AM makes the alloying elements susceptible to evaporation during processing. Magnesium has a high vapor pressure and is more susceptible [48].

3.1.2 Effect of powder characteristics

The morphology of the powder highly influences the quality of the builds. ***Figure 11*** shows the morphology of the powder used in LENS®. Most of the particles are spherical. Some elongated particles can be observed as well. The particles do not show a smooth surface, as seen in ***Figure 12***. Many particles can be observed to have some satellites. Satellites are particles sticking to the surface of the processed material. They can be formed by laser spattering or partial re-melting of the powder [49].

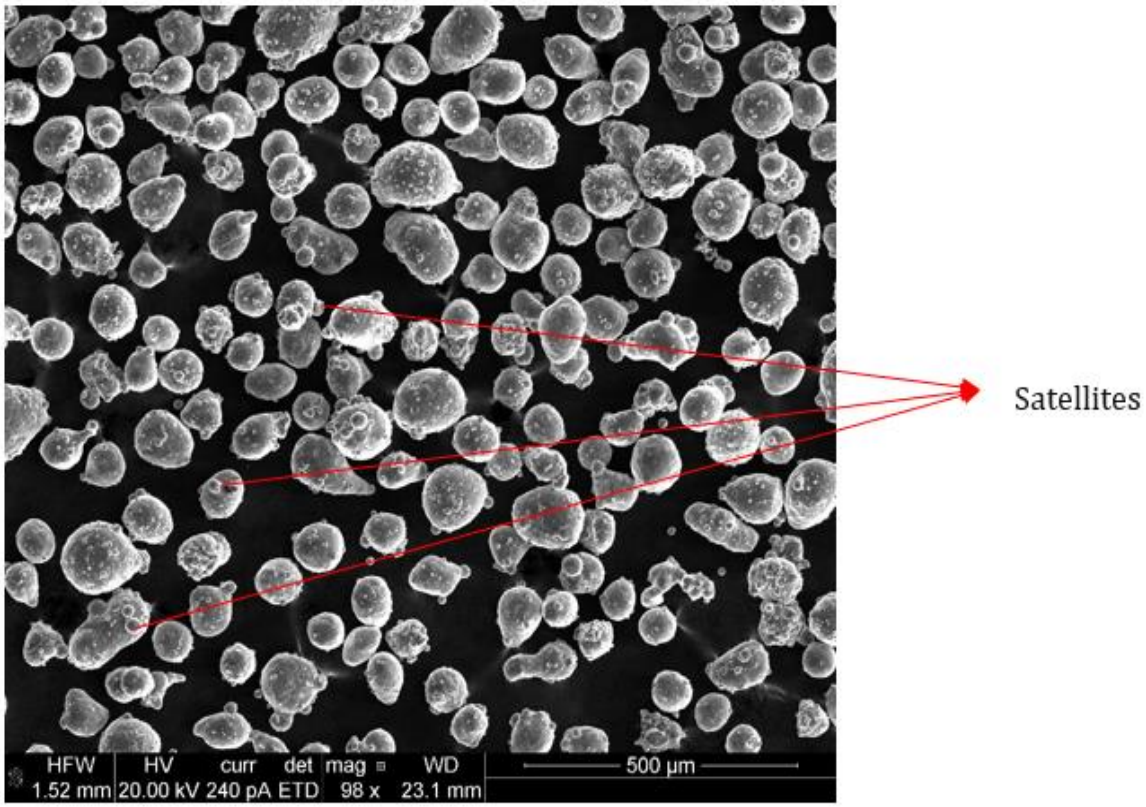

Figure 11 Morphology of the powder processed in LENS®

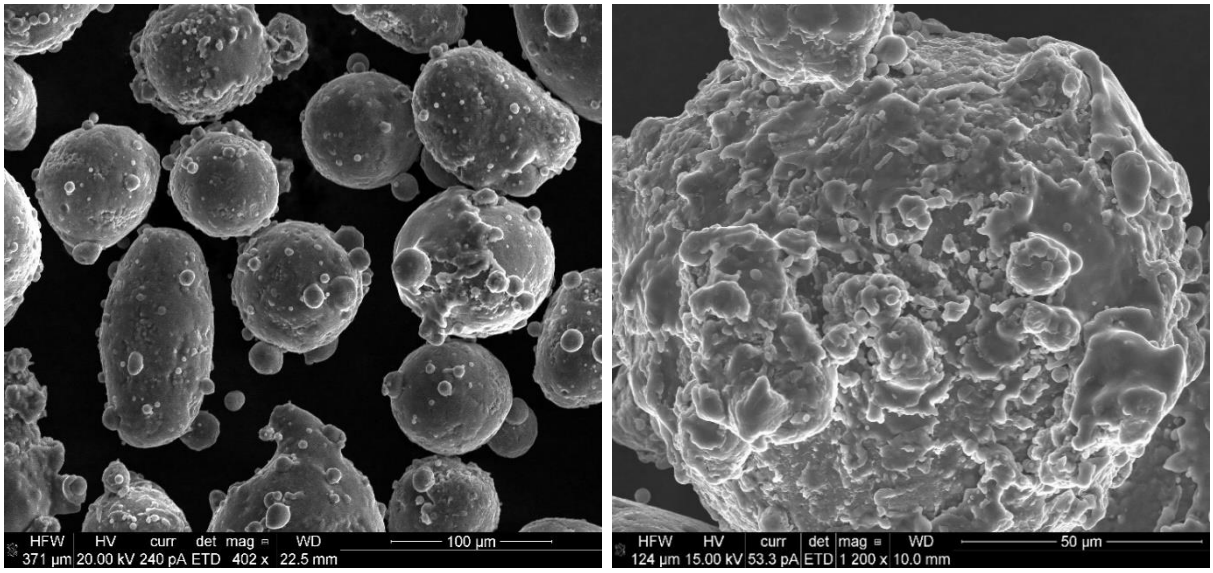

Figure 12 Irregularities on the surface of the particles

A good flowability and packing density is required to achieve good densification in the final parts. Good flowability is also required to achieve constant layer thickness and ensure a uniform laser beam absorption in the building area [50]. Of all the shapes, the spherical morphology with fewer irregular shaped particle allows for the best flowability and is the most desired for processing in AM [51]. Gas atomized powders usually produce spherical shape with smoother surface and lesser formation of satellites. The size distribution of the AlSi10Mg powder processed in LENS® was 40-100 μm. A wider particle size distribution with finer particle allows for better packing density as the void fraction will get filled effectively through particles of different sizes. However, finer particles lead to poor flowability in powder. Hence a compromise is required to achieve good flowability and packing density [23].

The composition of the powder also plays a significant role in the quality of the parts. Contaminants such as oxides, organics and moisture can affect the densification of the parts which in turn can affect the mechanical properties of the parts. The presence of oxides not only result in the formation of porosity but also reduces the wettability giving rise to defects such as balling. Li et al., [52] reported a significant increase to 99% in the relative density of the Al-12Si parts after a drying treatment of the powder in air at 100 ^{o}C for 1 hour.

Magnesium is added as a ternary alloying element to improve the strength of Al-Si alloys through precipitation hardening. The temperature within the melt pool is known to reach 1000 ^{o}C at the center and 600 ^{o}C at the edge [51]. This may cause evaporation of the alloying elements such as magnesium. This affects the age hardening response through the formation of the Mg_2Si precipitate may be severely affected.

3.2 Phase Identification

3.2.1 XRD

Figure 13 shows the XRD spectra of the as-built LENS® sample. The FCC α-Al characteristic planes (111), (200), (220) and (311) are seen in the pattern. The diamond cubic Si (111), (220), (311) planes are also observed, indicating the presence of silicon secondary phase. Weak signals of the FCC Mg_2Si phase are also observed. ***Figure 14*** shows the XRD spectra of the as-deposited SLM sample. The diffraction pattern was similar to that of the as-deposited LENS® sample. The characteristic FCC α-Al planes (111), (200), (220) and (311) are seen in the diffraction patterns. The diamond cubic Si (111), (220), (311) planes are also observed. The Mg_2Si phase is also observed in the as deposited SLM samples.

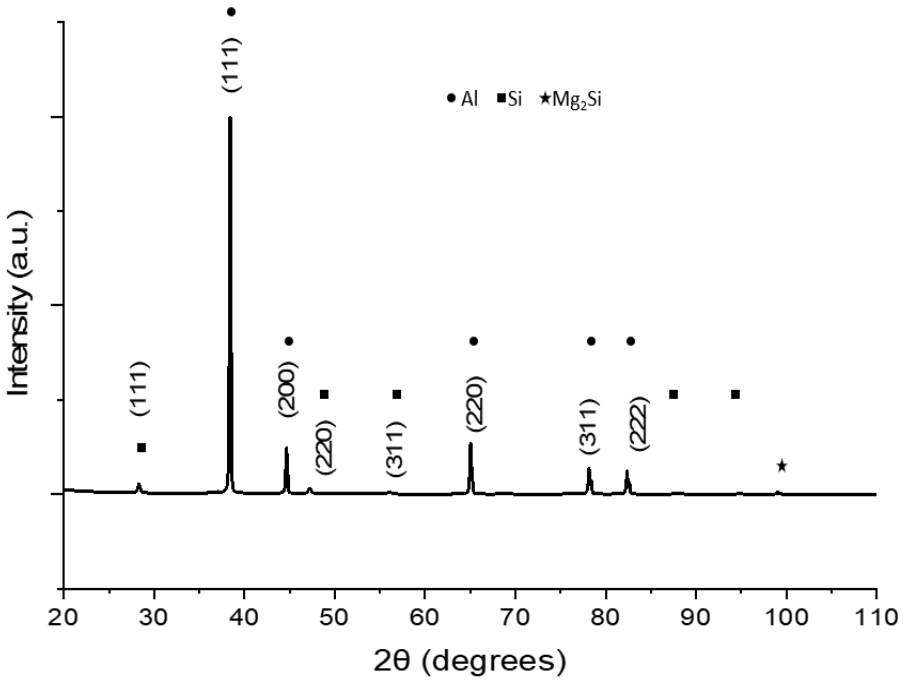

Figure 13 XRD pattern of as-deposited LENS® sample

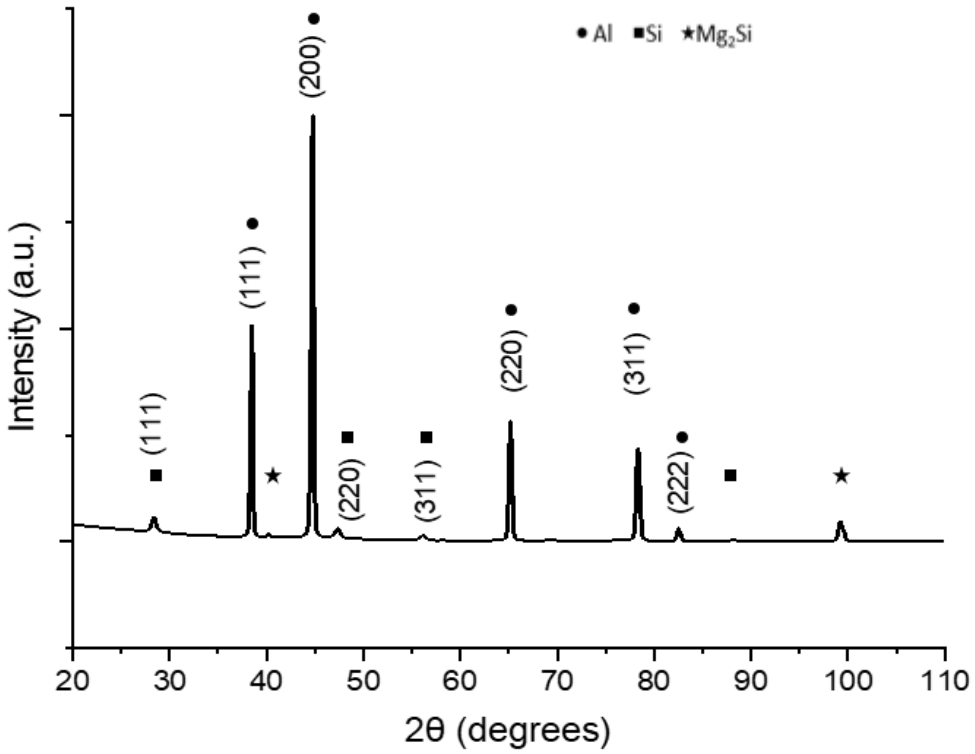

Figure 14 XRD pattern of as-deposited SLM sample

The peak corresponding to the (200) plane of FCC α-Al is the strongest in the SLM deposited sample, while the (111) plane peaks are the strongest in the LENS® as-deposited sample. This suggests a difference in preference for crystallographic orientation in both samples.

Texture depends on several factors including processing conditions, solidification, annealing and phase transformation [32]. Crystallographic texture refers to the preferential growth of grains in a certain crystallographic direction over others. In AM processes, the heat flow is highest along the -z direction towards the substrate. Hence solidification of the columnar cells occurs along this direction. The AM processes have a cellular mode of solidification in which the FCC crystals prefer growing in the <100> direction. But Thijis et al., [32] reported

that the texture in SLM processed AlSi10Mg alloys can be controlled though different scanning strategies. There was a reduction of 35% in texture from the unidirectional scanning to the alternating 90^{O} rotation scanning. The LENS® deposited sample had a rotation of 90^{O} after each layer and the SLM processed sample had a unidirectional scanning strategy. This difference in scanning strategy could be the reason for different Al characteristic planes having stronger peak intensities in the respective XRD patterns for the LENS® and SLM as-deposited samples.

3.2.2 DSC analysis

The precipitation of the Mg_2Si phase in the as-deposited sample has not been well studied in the literature. While there have been some reports [53], [54] of the detection of the Mg_2Si diffraction peaks in as-deposited LENS® and SLM AlSi10Mg samples, some authors have reported the absence of Mg_2Si peaks in the diffraction pattern of the as-deposited samples [55]. The high cooling rates may suppress the precipitation of Mg_2Si in the as-deposited samples. Abhoulkair et al., also reported evaporation of some Mg at a laser power of 100 W [23]. In our study, both the LENS® and the SLM processes employed laser powers greater than 100 W for deposition.

In our study, weak intensities of Mg_2Si peaks are detected in both the LENS® and SLM as-deposited samples. To support this finding and further understand the nature of the precipitation, DSC analysis was done on the as-deposited LENS® and SLM samples. In DSC, the amount of heat flow released or absorbed by the sample with increasing temperature is measured. Breaking of bonds requires supplying energy and the formation of new bonds releases energy. A precipitation reaction results in an exothermic reaction, and a dissolution

reaction results in an endothermic reaction. The nature of the peak defines the exothermic and endothermic reaction and is indicated along the axis.

Figure 15 and ***Figure 16*** show the DSC scans for the as-deposited LENS® and SLM samples, respectively. In the DSC scan of the LENS® as-deposited sample, an exothermic and endothermic peak are visible with maximum temperatures at 249 ^{o}C and 320 ^{o}C, respectively. Due to the limited literature available on the DSC analysis of AlSi10Mg processed through AM, DSC on the AlSi10Mg powder was done to understand the nature of these peaks.

Figure 17 shows the DSC scan for the virgin powder. An exothermic peak is seen at approximately 247.5 ^{o}C. This main peak is similar to the peak A observed in both the LENS® and SLM deposited samples. This suggests that it is associated with the intrinsic properties of the studied alloy. From the literature, it is characterized as the peak associated with the formation of Mg_2Si precipitates [56].

The peak B in the thermograms of the LENS® and SLM as-deposited samples is not observed in the thermogram of the powder. This suggests the peak is associated with the process. The exothermic energies of the peak vary due to the difference in processing conditions between the LENS® and SLM. This peak lies in the range of bulk interdiffusion of Si in Al [56].

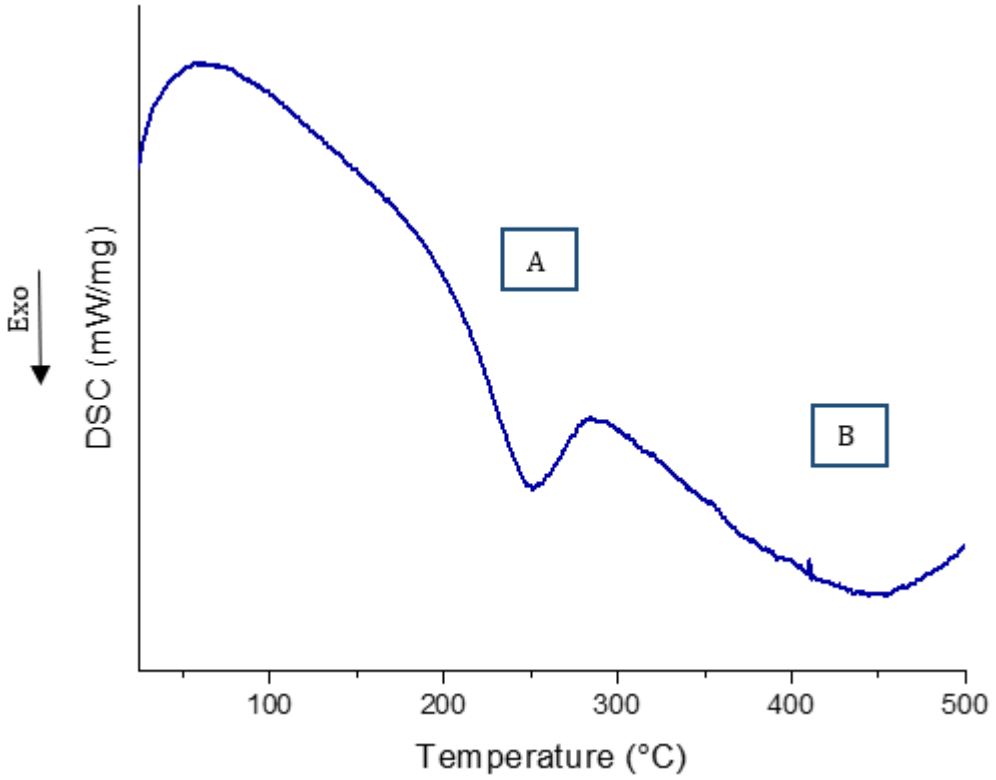

Figure 15 DSC of as-deposited LENS sample

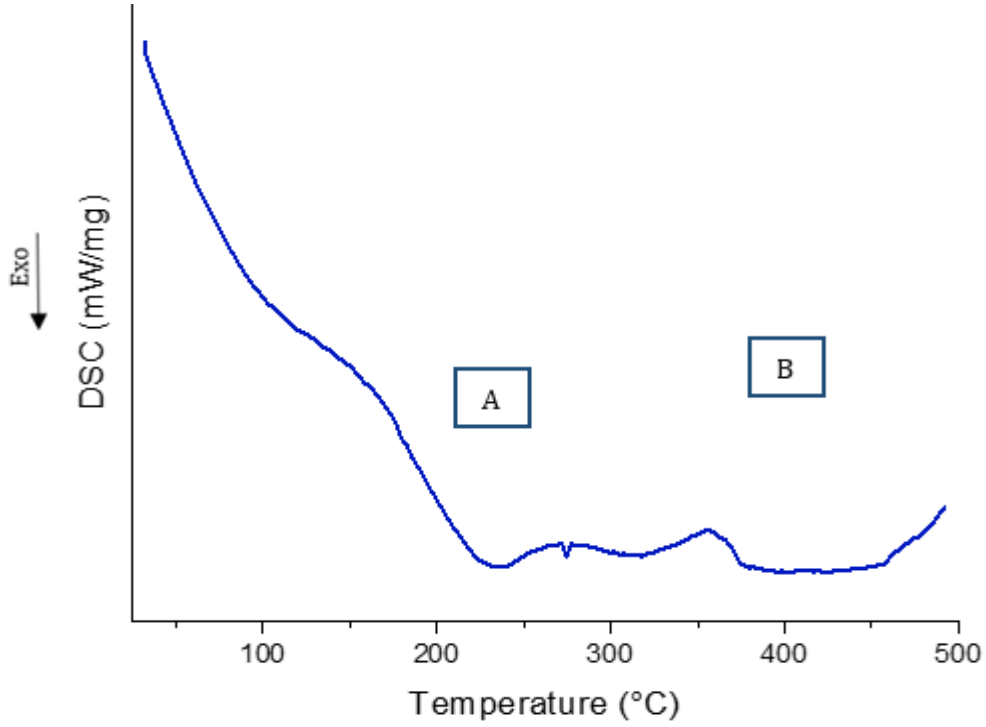

Figure 16 DSC of as-deposited SLM sample

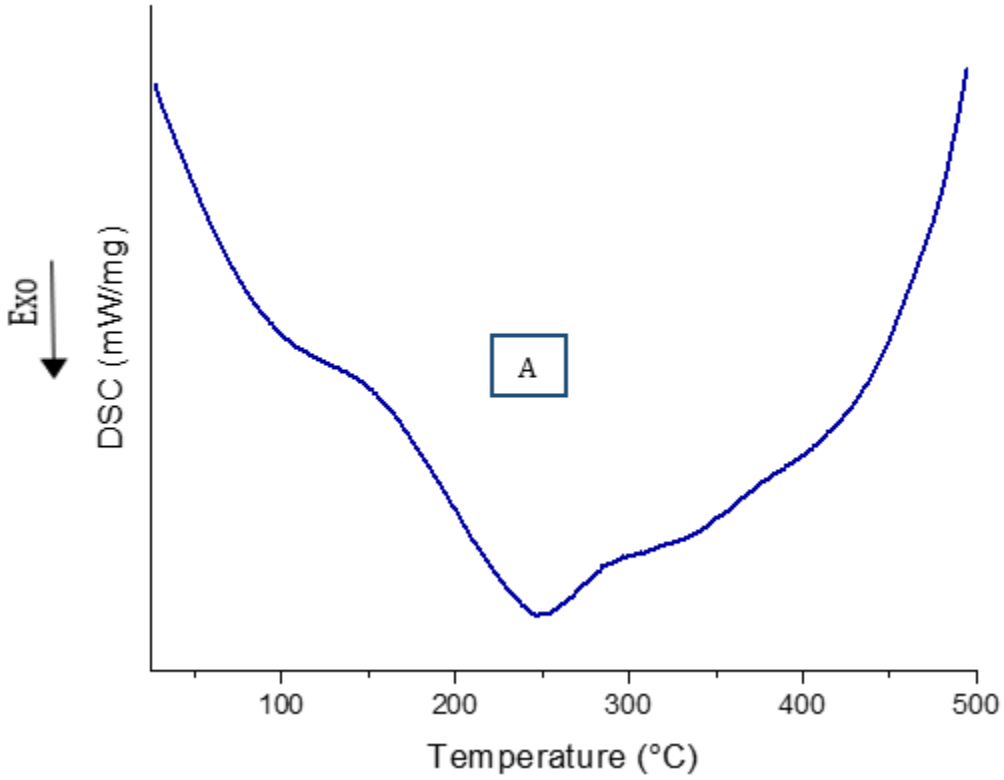

Figure 17 DSC of virgin powder

DSC analysis of as-deposited samples annealed at 190°C, 215°C, 250°C, 320°C for 1 hour was studied, as seen in ***Figure 18***. This study was used to understand the temperature range within which Mg_2Si precipitation occurs and determine the temperature range for subsequent in-situ experiments.

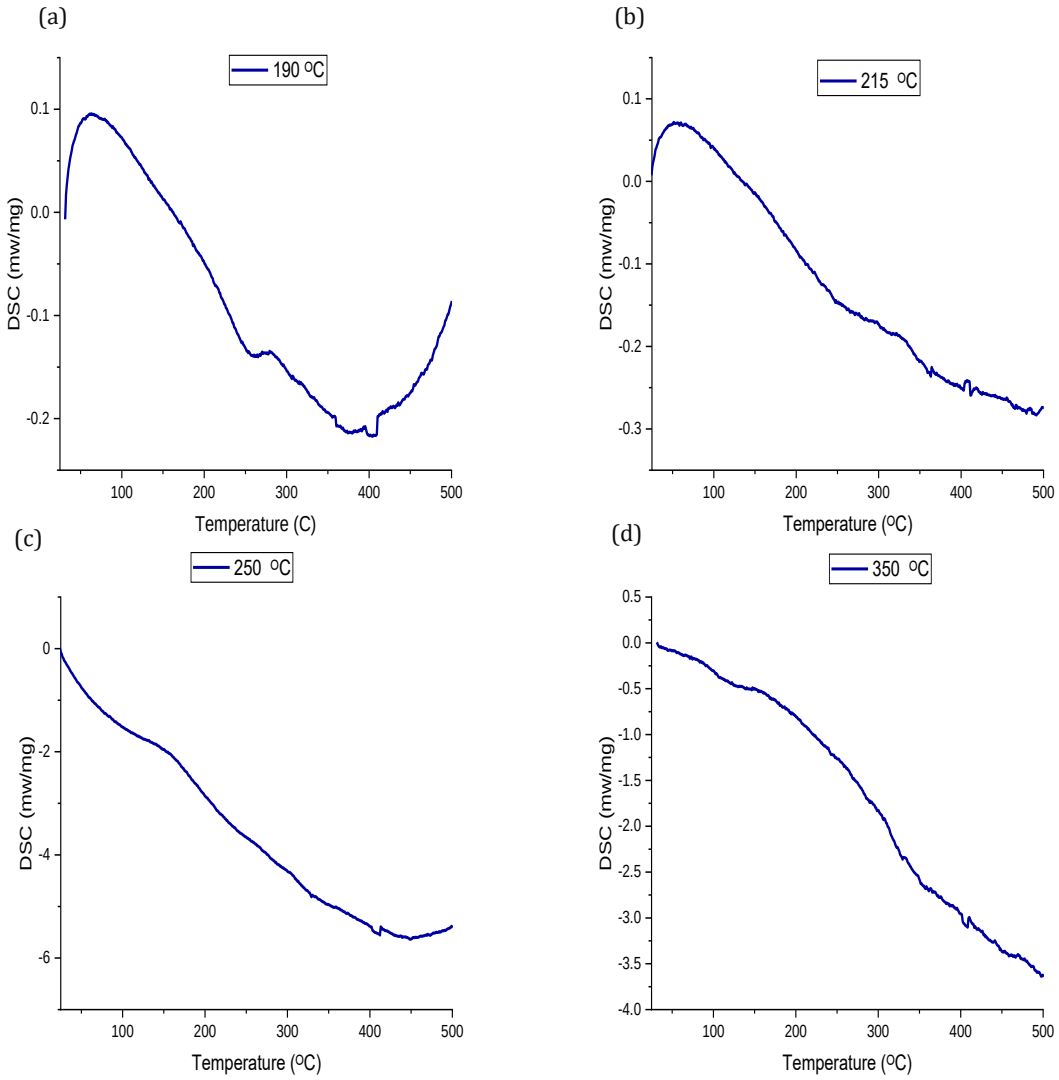

Figure 18 DSC of as-deposited LENS ® samples annealed at: (a) 190 °C (b) 215 °C (C) 250 °C (d) 350 °C

Figure 18(a) is the DSC curve for a sample after annealing at 190 °C for 1 hour. The area under the dip of the Mg_2Si precipitation peak (Peak A) for the as-deposited LENS® sample is 55.73 J/g. The DSC of the sample annealed at 190 °C has shown a reduction in area under peak A to 2.39 J/g. This reduction in area under peak A suggests that some of the Mg_2Si has precipitated out during the low temperature annealing, but the precipitation reaction was not complete. The area under peak B is still close in value to the area under the peak B of the as-deposited

sample. This shows that the diffusion of silicon from the α-Al has not started. In ***Figure 18(b),*** , peak A of the sample annealed at 215 ^{o}C shows a further reduction in area to 0.531 J/g.

Figure 18 (c) and ***Figure 18 (d)*** show the DSC curves for the sample annealed at 250 ^{o}C and 320 ^{o}C. Peak A disappears completely indicating the completion of the precipitation reaction.

3.3 Microstructural Study of the LENS® and SLM deposited samples

3.3.1 Microstructure of the melt pool

Figure 19 shows low magnification images of an unetched LENS® sample viewed along the YZ plane, which is parallel to the build direction, and the XY plane, which is perpendicular to the build direction. The half cylindrical melt pool boundaries overlap across the different layers as the laser source moves and melts the material. The width of the melt pool is approximately 300 μm, which is close to the laser spot size. The alternating scanning direction (90^{O} hatch rotation) after each layer can be seen in the melt pool boundaries. The figure highlights the scalloped geometry of the melt pools in a single layer where the scanning direction was normal to the sample face. The scanning direction of the next layer was parallel to the sample face such that the view is of a length-wise cross-section of a single track. This pattern is repeated from the substrate to the top of the build [57]. This type of geometry has been reported for Al-Si alloys and is also observed in stainless steels and Ti alloys [58], [59]. The XY plane shows the elongated elliptical shape of the melt pool from the top.

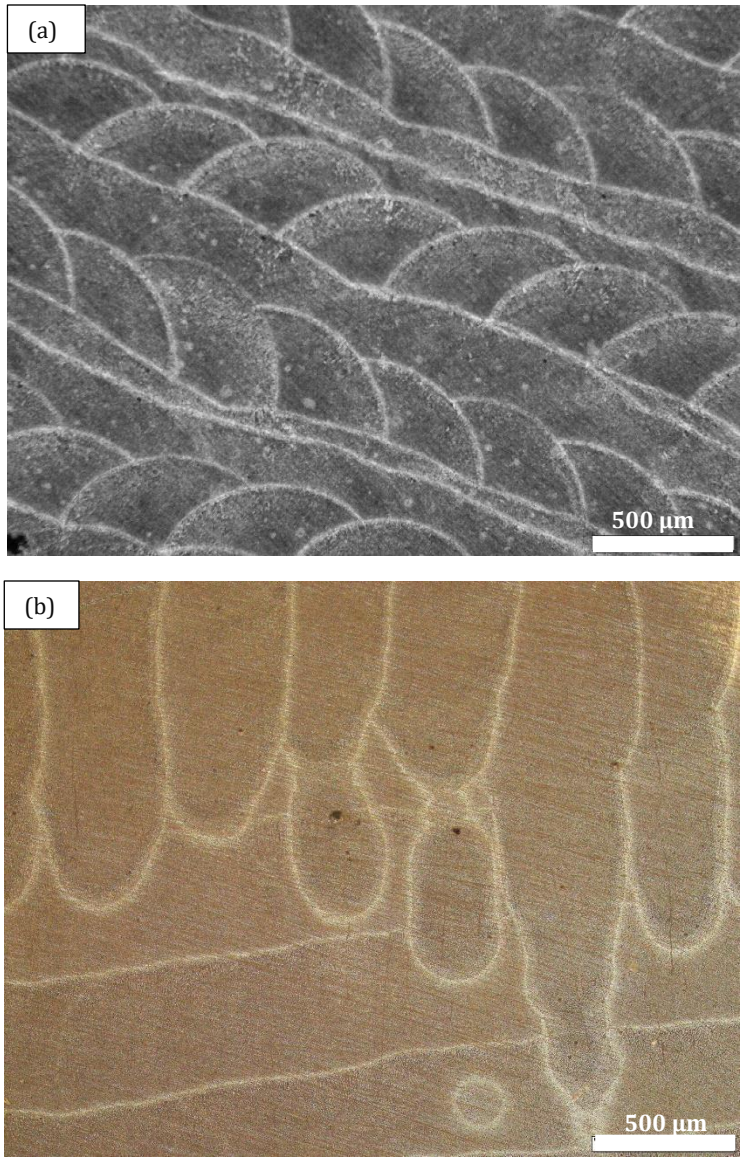

Figure 19 Low magnification images of the melt pools in the as-deposited LENS® sample along: (a) YZ plane (b) XY plane

Figure 20 shows the melt pool boundaries of the SLM deposited sample along the YZ plane. The unidirectional scanning strategy gives a uniform scalloped shape to the melt pool in each layer. The width of the melt pool is approximately 100 µm and smaller than the width of the melt pool in the LENS® deposited sample due to the different process parameters [60].

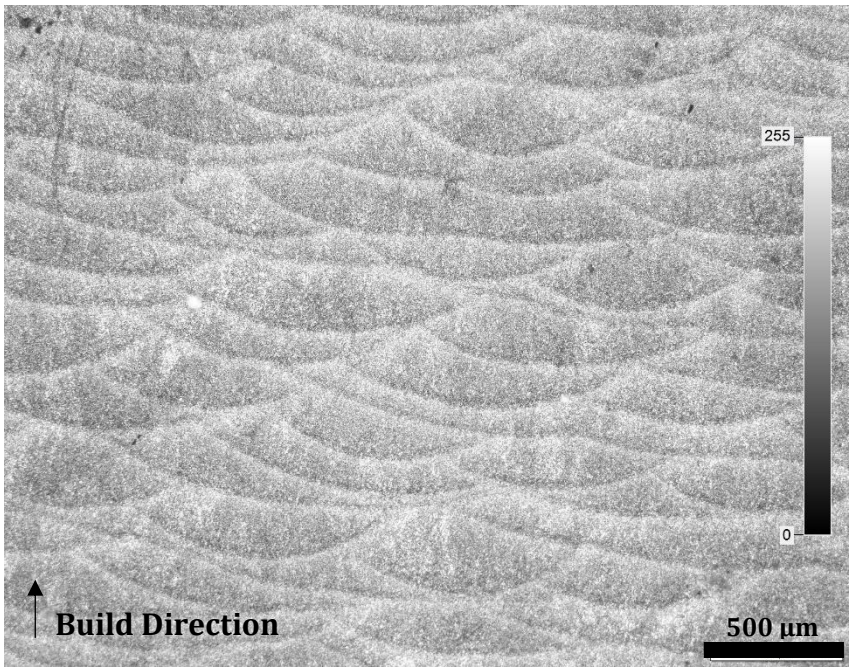

Figure 20 Low magnification image of the as-deposited SLM sample

Figure 21 shows higher magnification images of the microstructure of an etched LENS® deposited sample viewed along the YZ plane. The melt pool boundary is highlighted by the red dashed curve. A eutectic microstructure is observed with a fine dispersion of silicon in the aluminum matrix. The solidification microstructure depends on the thermal gradient. There are three distinct regions within the melt pool. The core of the melt pool has finer equiaxed structure and the region near the melt pool boundaries show a coarser columnar grain growth. There is a transition region in between where the eutectic silicon network is disconnected. ***Figure 22*** is a higher magnification SEM micrograph showing the three regions.is a higher magnification SEM micrograph showing the three regions.

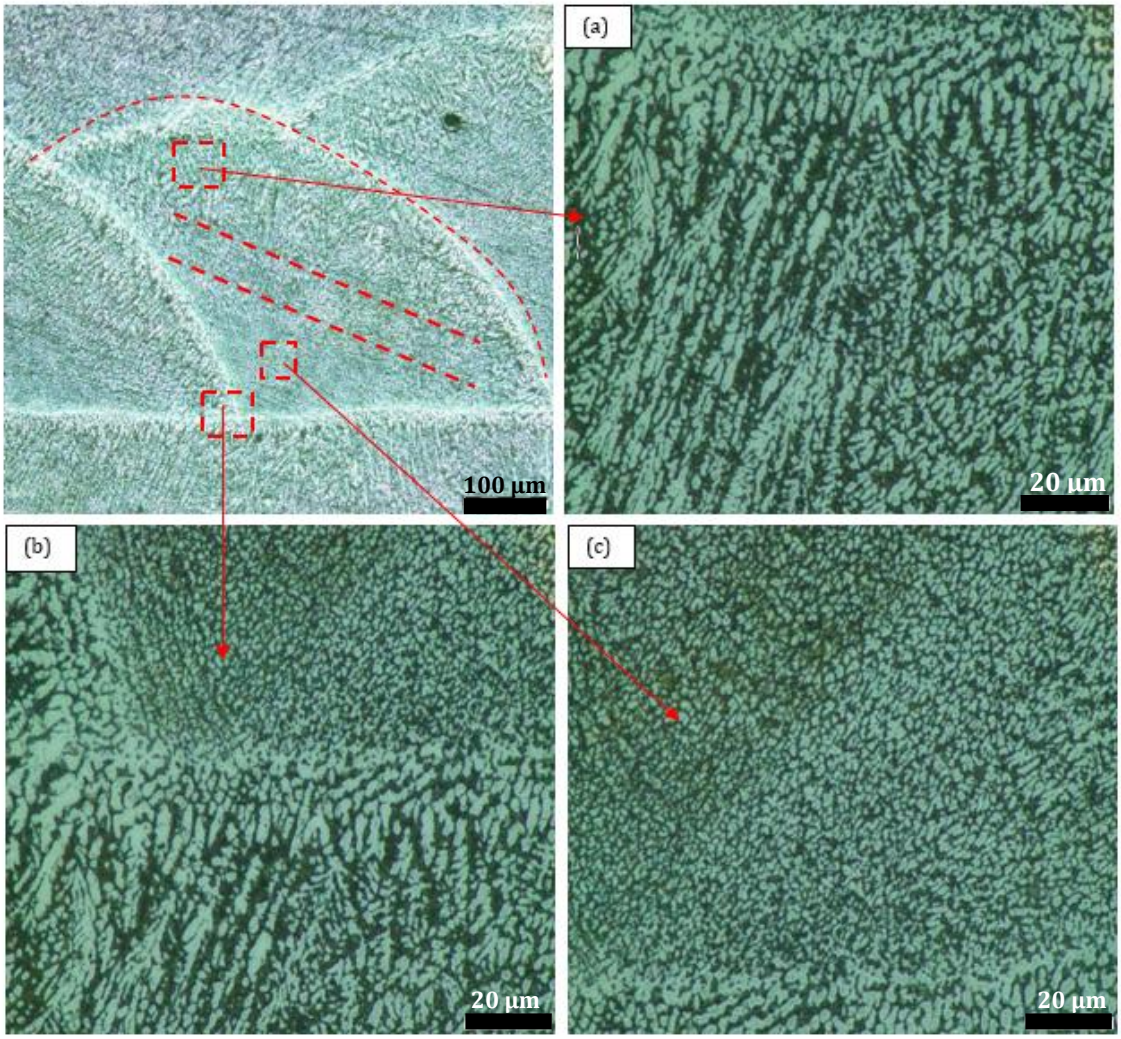

Figure 21 Distinct regions in the melt pool of the as-deposited LENS ® sample: (a) Coarser columnar grains along the melt pool boundary (b) Transition between the equiaxed and columnar region (c) Finer equiaxed grains at the core of the melt pool

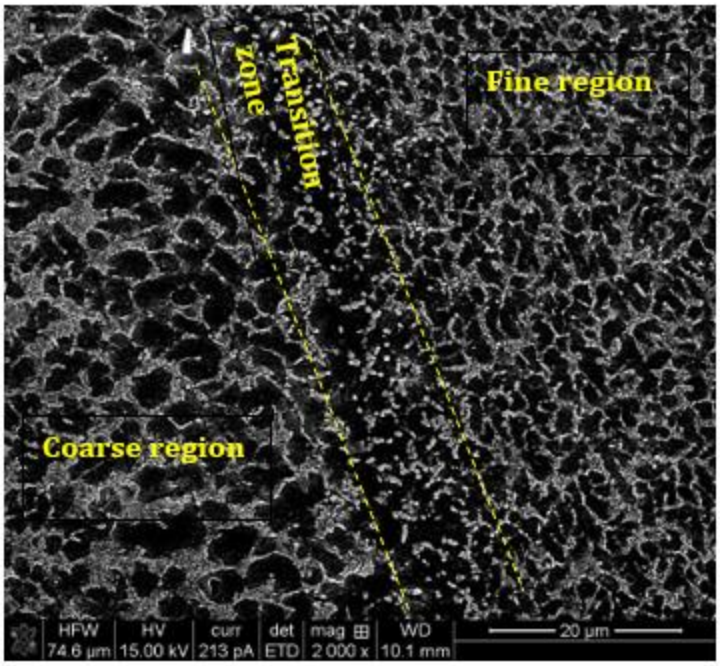

Figure 22 Higher magnification image of the three regions in the as-deposited LENS® sample

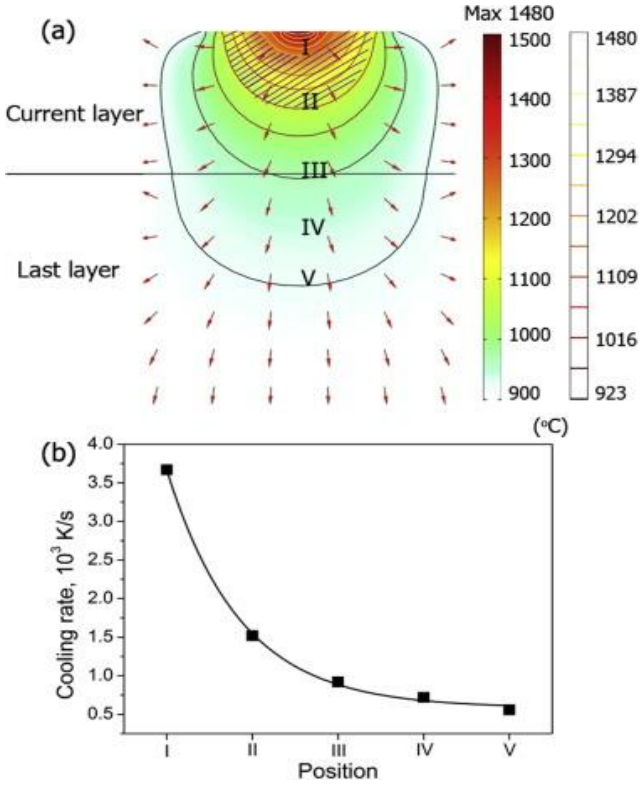

Figure 23 Evaluation of the change in cooling rate across the melt pool using FEM [56]

The melt pool core and boundary experience different thermal histories. X.P Li et al., [61] used Finite Element Modelling in SLM of Al-Si alloys to calculate the change in gradient and cooling rate across the melt pool, as shown in ***Figure 23***. The melt pool core is hotter than the boundary and is surrounded by the molten liquid and solidifies as a fine equiaxed microstructure. The boundaries are in contact with the solidified material from the previous layer and solidify at a slower rate and have a coarser structure. The partial re-melting of the previous layers give rise to epitaxial growth.

Figure 24 shows the microstructure of the as-deposited LENS® sample along the XY plane and YZ plane characterized in SEM. The microstructure shows a fine fibrous distribution of eutectic silicon in the aluminum matrix. The morphology of the silicon phase is very different from the needle or plate shaped morphology in castings [62] . The cells appear equiaxed when viewed along the XY plane and elongated along the YZ plane. The EDS mapping of the as-deposited LENS® sample is shown in ***Figure 25*** confirming the presence of Si. The Mg phase is too fine to be identified in SEM.

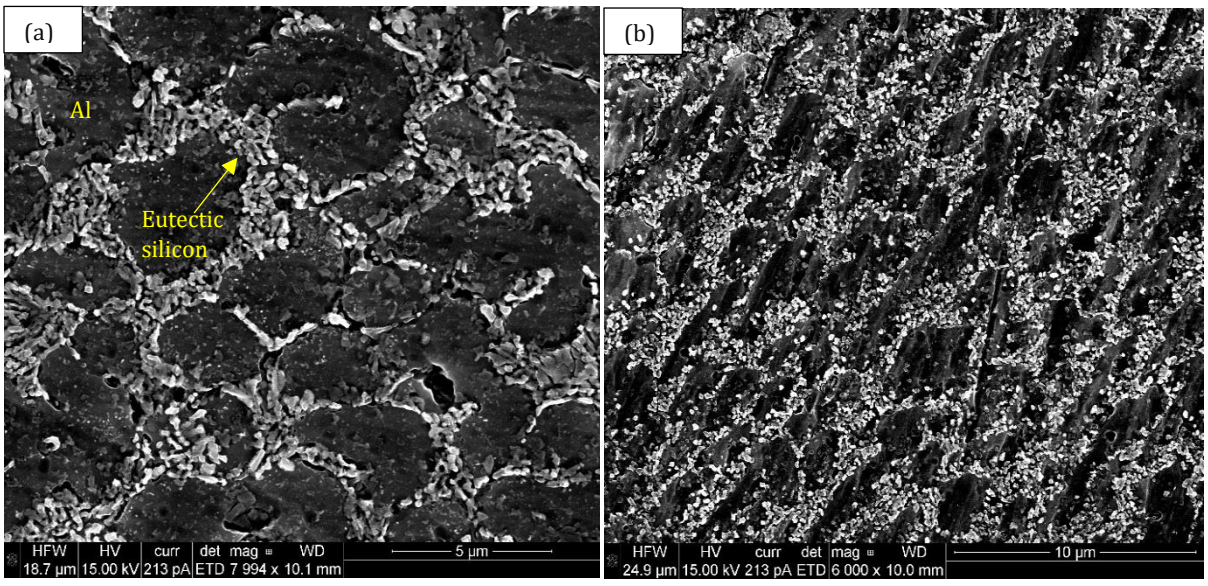

Figure 24 SEM microstructure of the as-deposited LENS® sample: ***(a) along XY plane (b) along YZ plane***

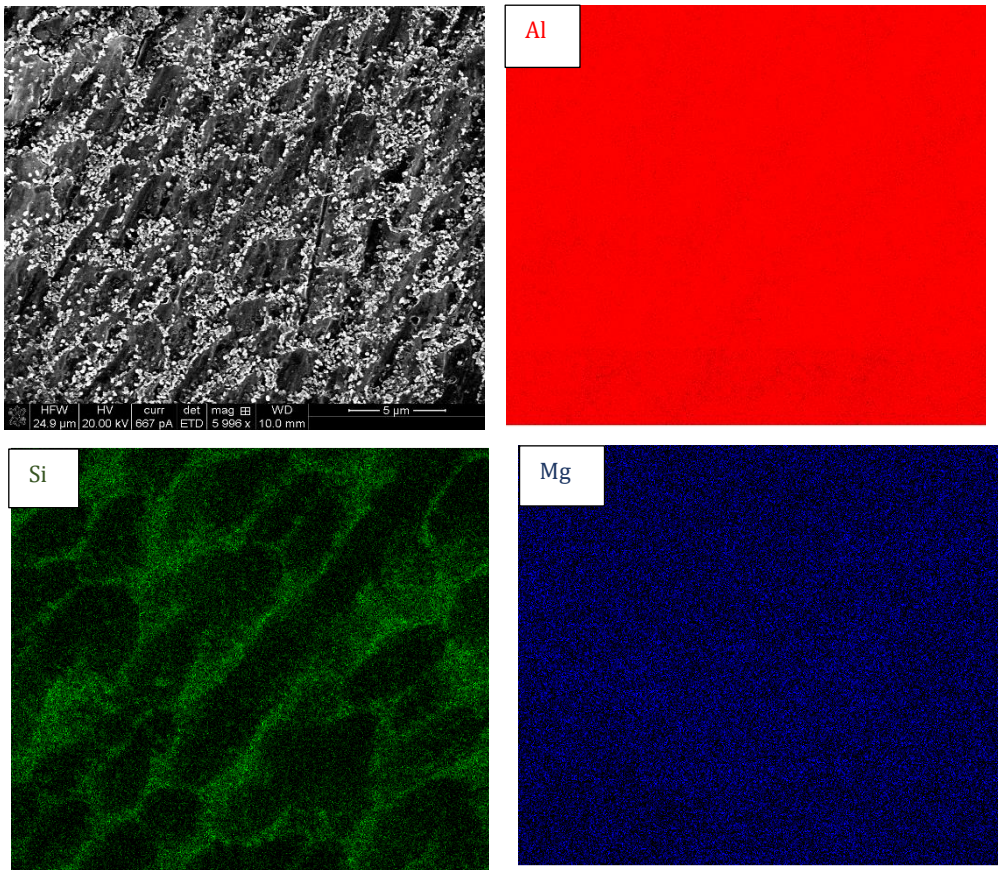

Figure 25 SEM-EDS mapping of Al, Si and Mg for the as-deposited LENS® sample

Figure 26 shows the phase diagram of Al-10wt.% Si -0.35wt% Mg. Upon solidification the alloy forms three phases – the α-Al phase, the needle-shaped Si phase and the β-Mg_2Si phase [63], [64]. The needle-shaped morphology is considered detrimental to castings and the morphology of the silicon is modified chemically or by changing the cooling rates [65]. Addition of Na or Sr is usually employed. The chemical modifications alter the growth mechanism of silicon by increasing the number of nucleation sites [64] and changing it to a spherical morphology.

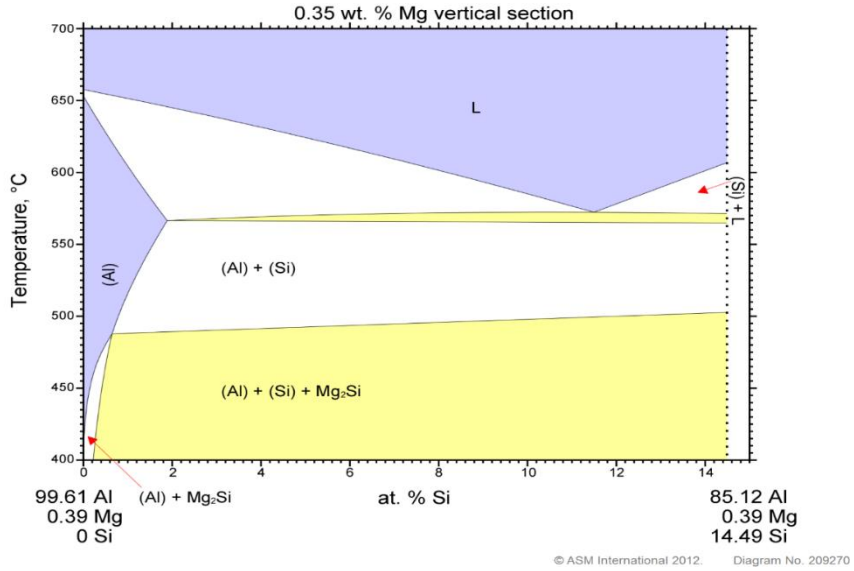

Figure 26 Vertical cross section of Al-Si phase diagram at 0.35 wt.% Mg [63]

The liquid/solid solidification front can be planar, cellular or equiaxed based on constitutional supercooling [66]. In AM processes the cooling rates are on the order of 10^3-10^6 K/s [7]. Previous studies have shown that the solid solubility of silicon in aluminum can be extended by high cooling rates [67]. This is attributed to the rapidly moving solidification front, which does not provide enough time for the silicon to diffuse. The silicon is trapped, and the aluminum matrix gets supersaturated.

The equilibrium solubility of silicon in aluminum is 1.67 wt.%, as seen from the phase diagram. Li et al., used TEM energy dispersive X-ray spectroscopy mapping and determined that the Si concentration in the as-processed SLM AlSi10Mg sample was 7 wt% [68]. The extended solubility decreases the concentration of solute in the liquid and increases the constitutional supercooling, resulting in a cellular morphology, as seen in **Figure 24**. The high

cooling rate forms nano-sized cells, which are too fine to be identified in SEM. The Mg_2Si precipitation hardenable phases are also too fine to be identified in SEM.

The microstructure of the as-deposited SLM sample is shown in ***Figure 27*** . The SLM sample also shows a fibrous network of silicon phase. The beam size and feature size are smaller in a powder bed fusion process than in a directed energy deposition technique [69]. Thus, the cooling rates are expected to be higher in SLM than in the LENS®. This gives an even finer cell structure for SLM than in LENS®. ***Figure 28*** shows the SEM-EDS mapping of Al, Si and Mg for the as-deposited SLM sample. The mapping confirms the presence of silicon along the cell boundaries and in the aluminum matrix. The Mg-rich phase is too fine to be identified in SEM, similar to the as-deposited LENS® sample.

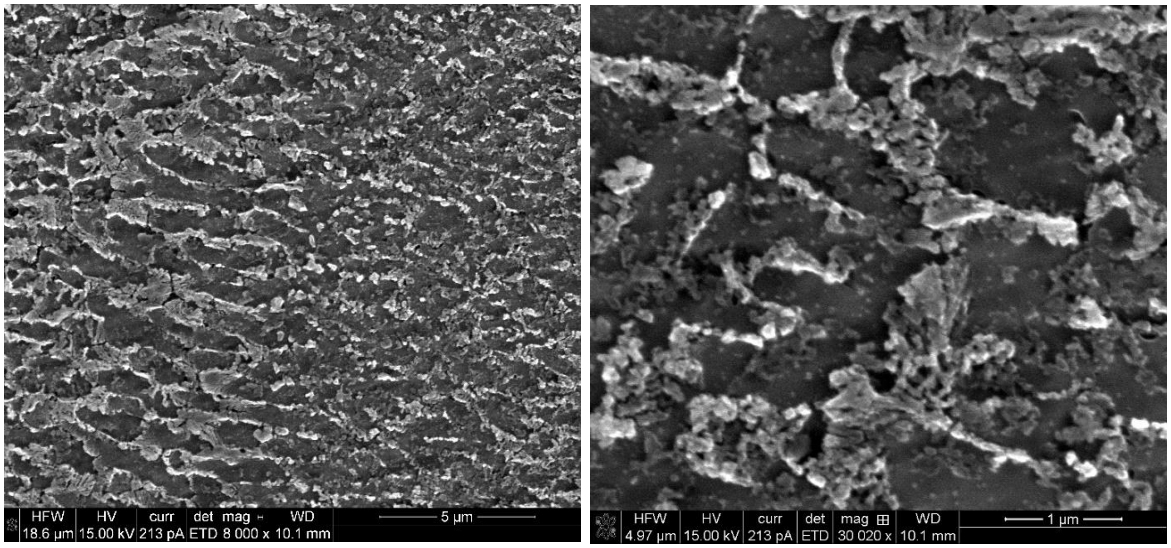

Figure 27 SEM microstructure of the as-deposited SLM sample

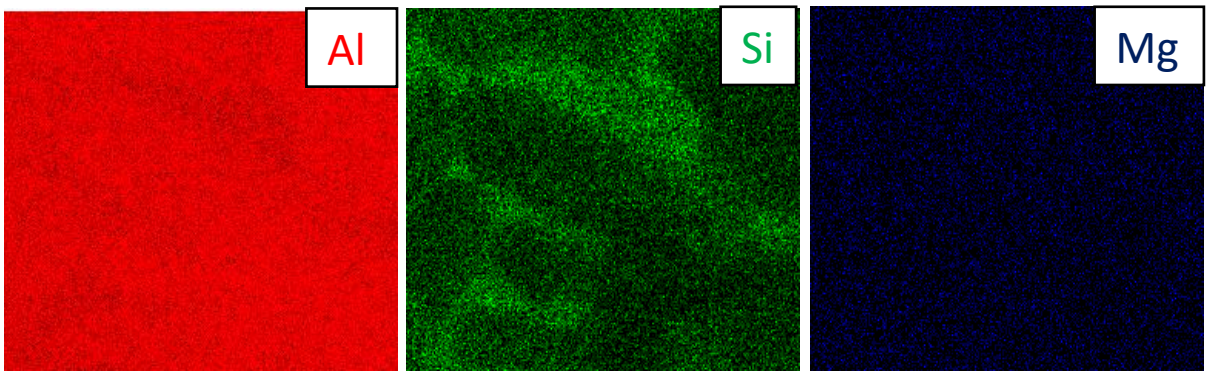

Figure 28 SEM-EDS mapping of Al, Si and Mg for the as-deposited SLM sample

3.3.2 TEM Characterization of the as-deposited LENS® sample

The resultant microstructure in AM processes are very fine due to the rapid solidification. Limited reports are available on the phases present after deposition. TEM analysis is required to characterize the morphology of the constituent phases. In this section the as-deposited LENS® samples are characterized in TEM.

Figure 29 shows the microstructure of an as-deposited LENS® sample, as characterized in TEM. Cells of size 1 – 2 μm are formed, which are very fine. The cellular dendrites formed in casting are approximately 400 μm [70]. These cell boundaries are decorated with silicon. The morphology of the primary silicon in hypoeutectic cast alloys are reported to be plate shaped, which is different from the morphology observed here.

A pure metal usually solidifies in the planar solid-liquid interface. This interface can be disrupted by increasing the constitutional supercooling. It was found for a planar interface to be stable, the following condition must be true [71]:

$$\frac{G}{R} \geq \frac{\Delta T}{D_L}$$

where G is the thermal gradient; R is the growth rate; ΔT is the freezing range and D_L is the diffusion coefficient of the liquid.

An increase in constitutional supercooling changes the solidification mode from planar to cellular, dendritic and equiaxed solidification modes, as shown in ***Figure 30*** [71]. The dependence of morphology and feature size on the thermal gradient and growth velocity of the solid liquid front can be understood through ***Figure 30***. The high thermal gradient in AM processes makes it fall under the cellular region highlighted in red. The high cooling rate also gives a very fine structure.

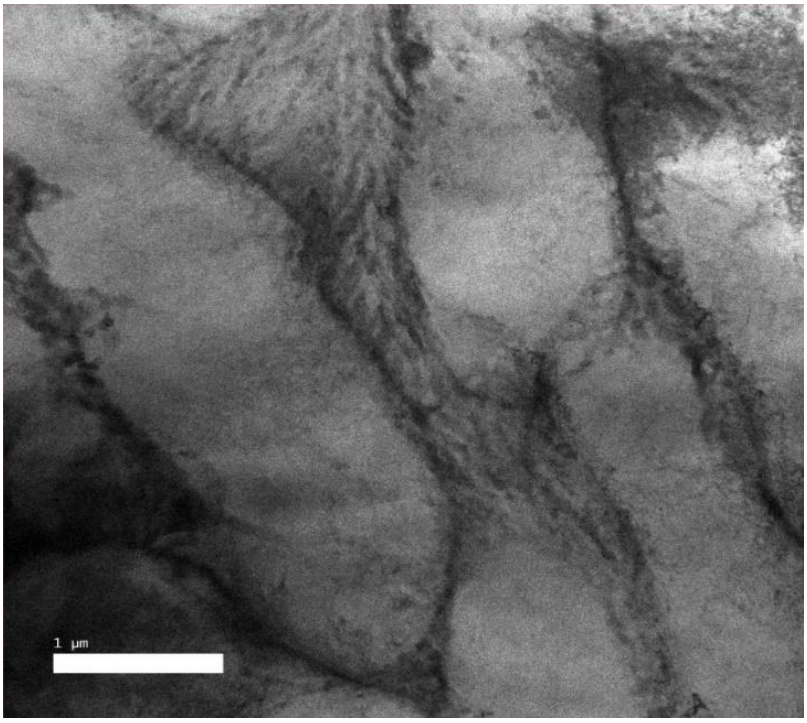

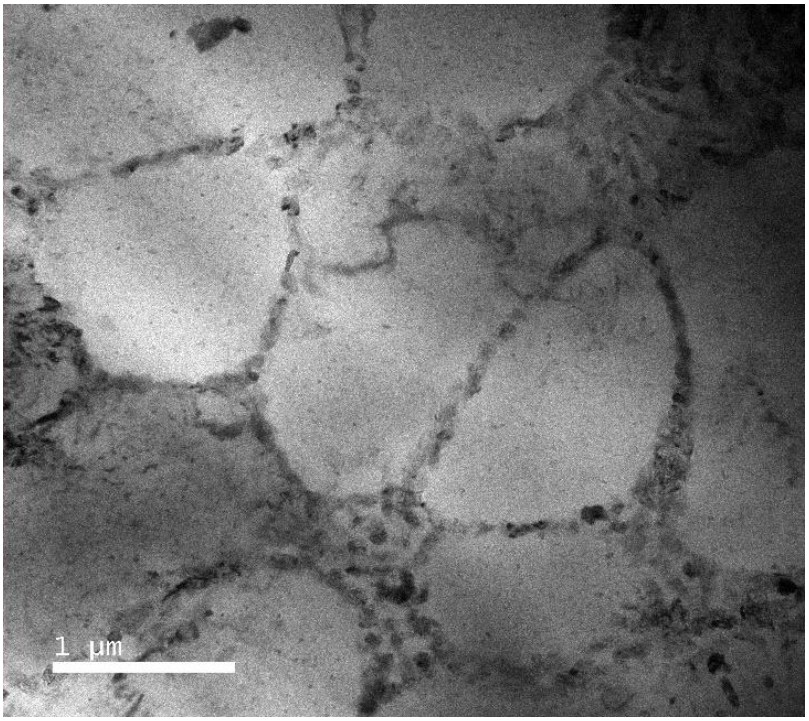

Figure 29 TEM characterization of an as-deposited LENS® sample

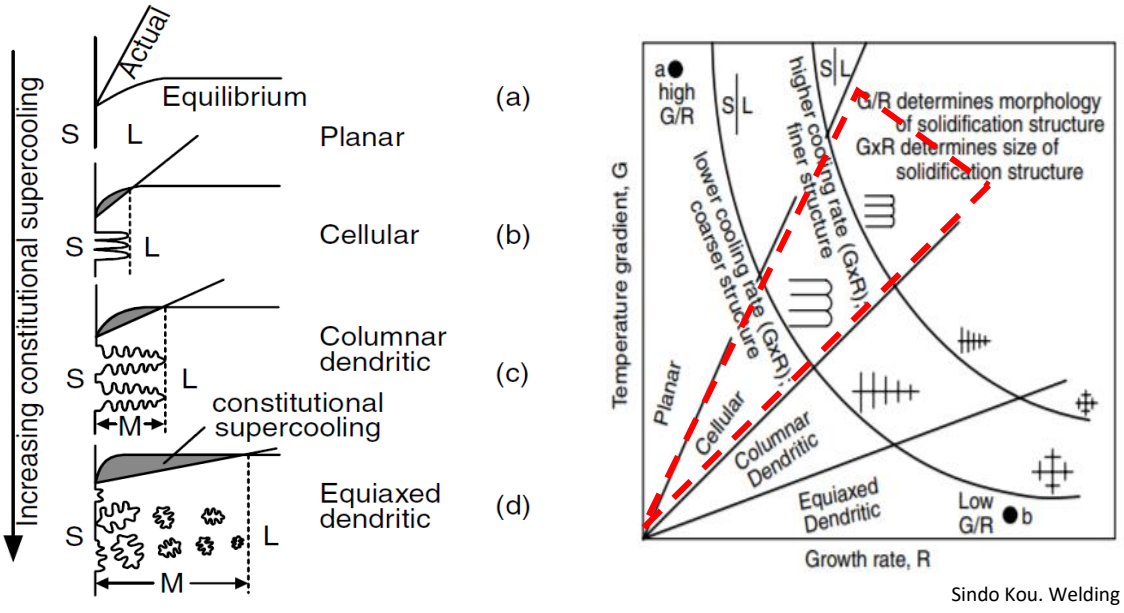

Figure 30 Dependence of microstructure on thermal gradient (G) and growth rate (R) [71]

Figure 31 shows the STEM-EDS characterization of the as-deposited LENS® sample. The EDS mapping shows the silicon along the cell boundaries. There is also segregation of Mg along the cell boundaries indicating the presence of Mg_2Si. The feedstock powder also contains some Fe, which also segregates along the cell boundary. Fe is identified as a common impurity in many AlSiMg cast aluminum alloys [72]. The powder contains Fe in concentration less than 0.15 wt%, but Fe has a very low solid solubility of 0.05 wt. % in Al [73]. Hence it is possible that Fe forms an intermetallic phase. From the literature, this phase is identified as the π-$Al_8Si_6Mg_3Fe$ phase [74].

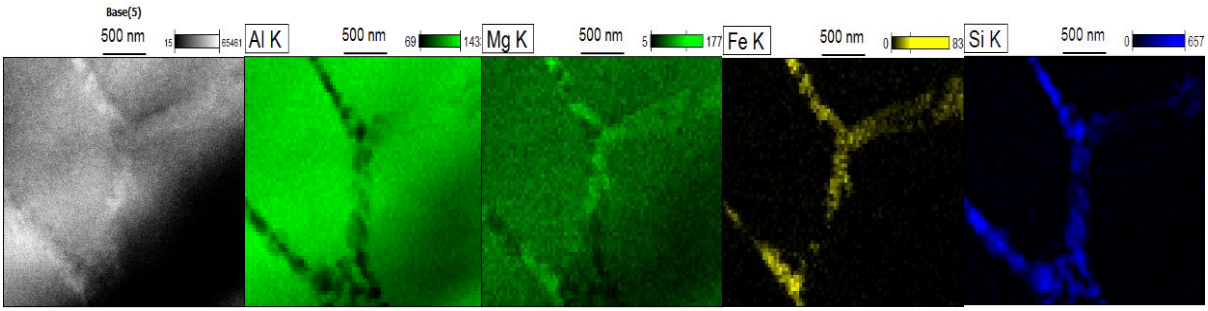

Figure 31 STEM-EDS characterization of the as-deposited LENS® sample

The EDS mapping shows the distribution of silicon throughout the matrix. Besides the eutectic silicon along the cell boundaries, numerous primary silicon particles are uniformly distributed within the cells, as seen in ***Figure 32(b) & (c)***. The size of the eutectic silicon is approximately 200 nm, whereas the primary silicon particles are less than 50 nm in size. Formation of primary silicon particles in hypoeutectic alloys has been observed in Al-10%Si cast alloys. In this, the primary silicon particles were observed to have a faceted morphology and a random growth preceding the formation of the eutectic silicon [75]. Further investigations are needed regarding the growth mechanism of the primary silicon particles in this case. The silicon particles within the cells are of two types, as seen in ***Figure 33***: rod

shaped and irregular shaped particles. The rod-shaped particles have a width of approximately 5 nm.

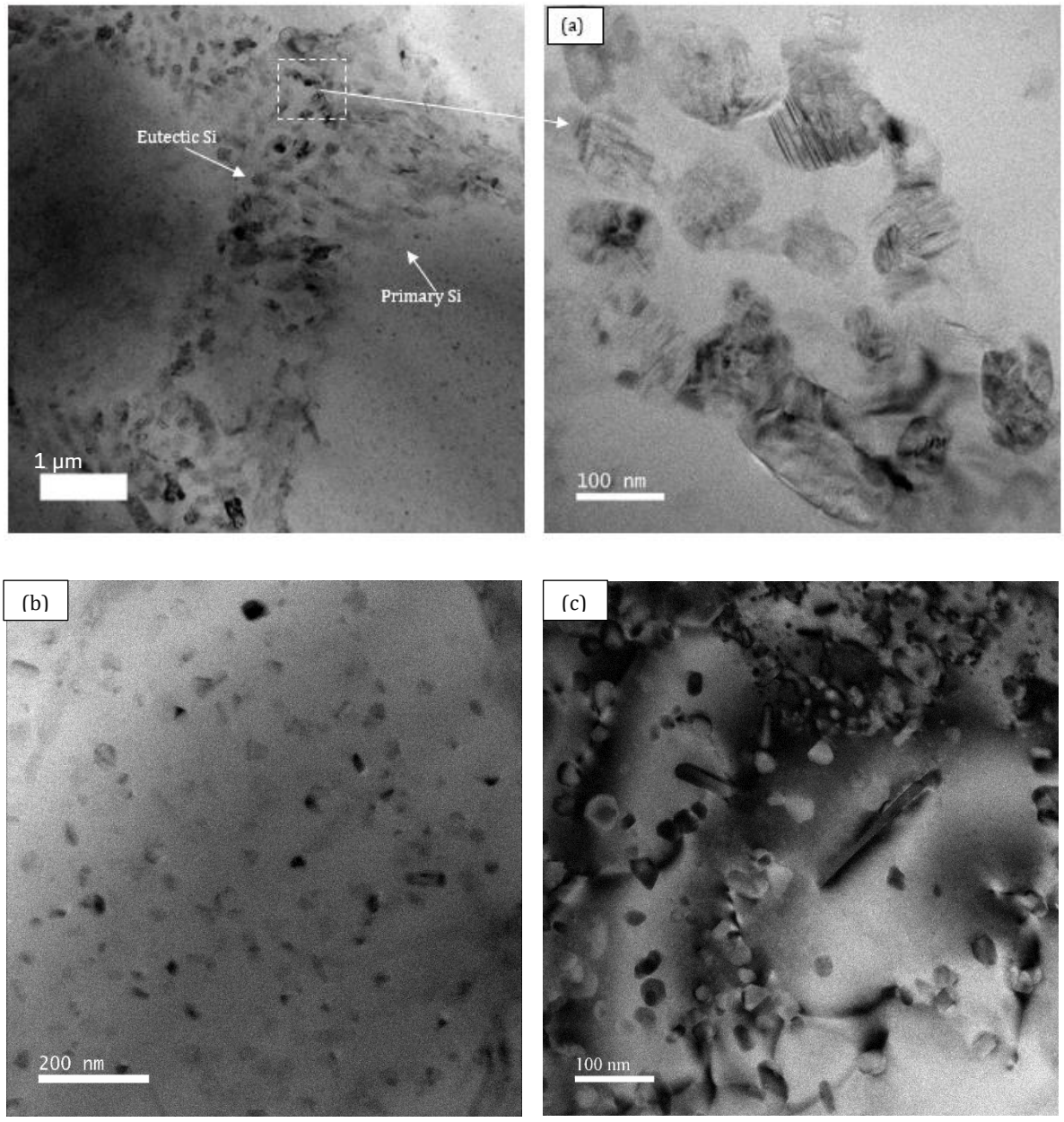

Figure 32 Distribution of silicon: (a) eutectic Si (b) & (c) BF and DF images of primary Si particles (*difference in scalebars)

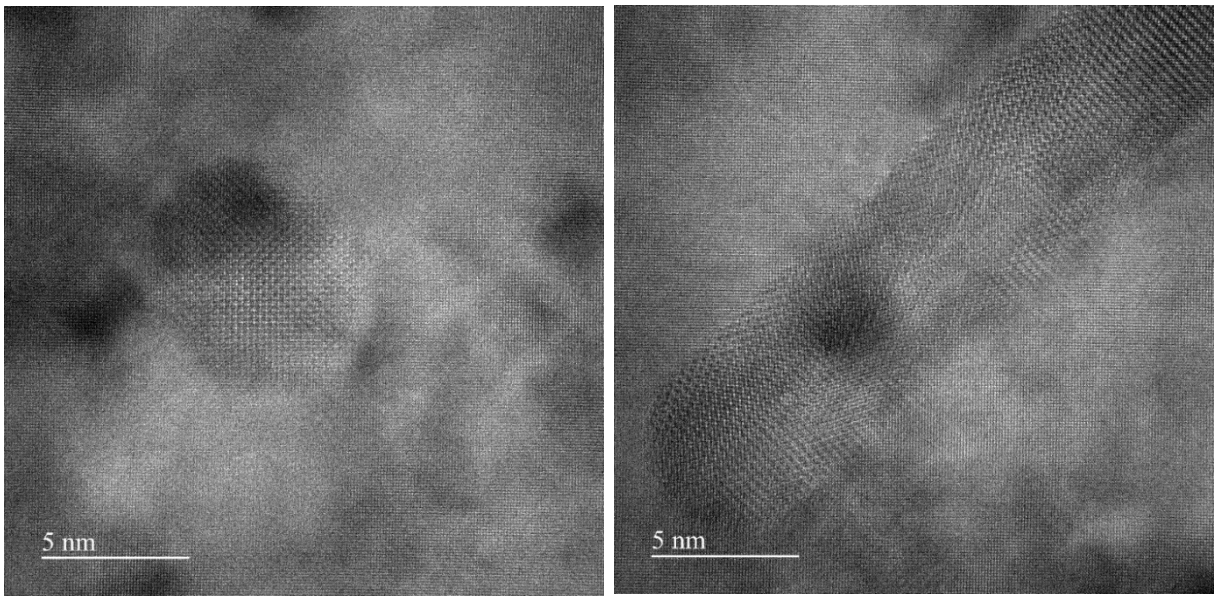

Figure 33 HRTEM of primary Si precipitates

3.3.2.1 Crystallographic orientation relationship in the as-deposited LENS® sample

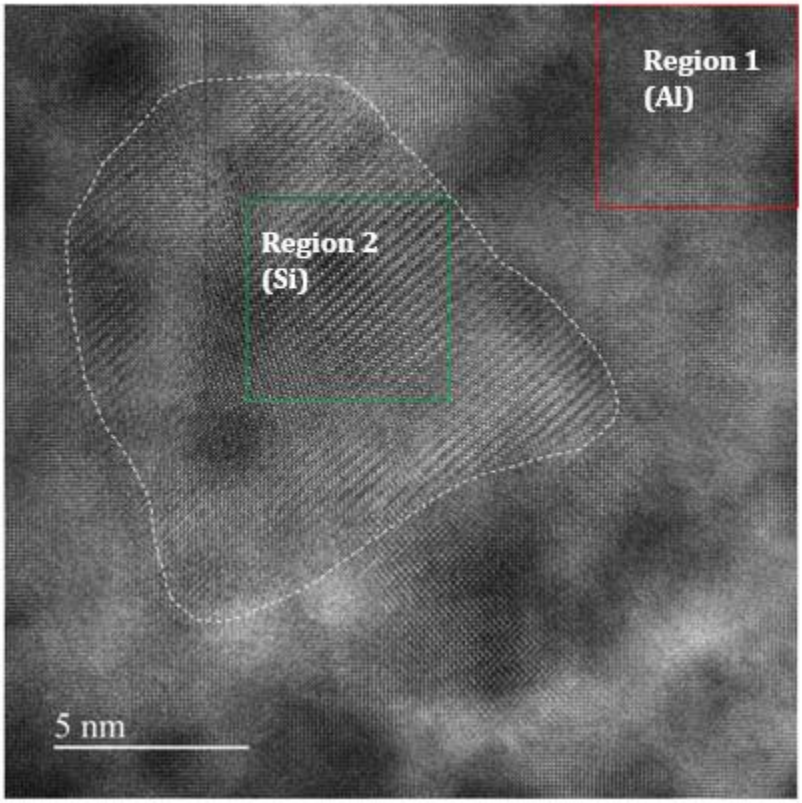

Figure 34 HRTEM of Si in an Al matrix along <001> zone axis

Figure 34 shows a HRTEM of the primary silicon and the aluminum matrix along the <001> zone axis of aluminum. The electron diffraction patterns taken from region 1 (Al) and region 2 (Si) are shown in ***Figure 35***. The primary silicon and the aluminum matrix have a coherent interface with a crystal orientation relationship of (020) Al || (220) Si. No specific relationship between the eutectic silicon and the aluminum matrix was found.

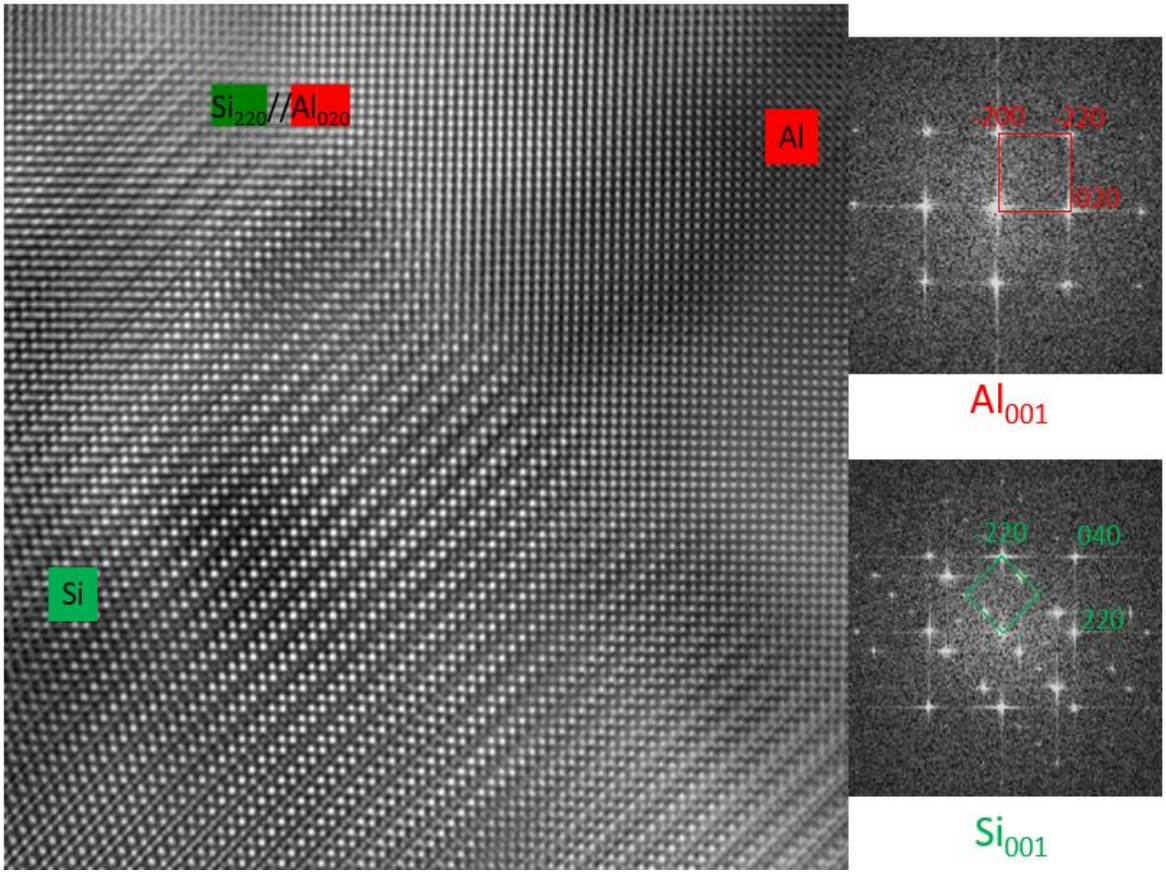

Figure 35 SAED pattern of (a) Al taken from region 1 (b) Si taken from region 2

3.3.2.2 Gradient in microstructure of the as-deposited LENS® sample

Figure 36 shows the cell microstructure of the as-deposited LENS® samples from two locations: top and bottom of the build, as shown in **Figure *10.*** The size of the cells increases from 1 μm at the top of the build to 1.5 μm at the sample taken from the bottom of the build. A finer distribution of eutectic silicon in the top of the build can be seen compared to that in the bottom of the build. The amount of primary silicon within the cells is smaller at the top than at the bottom, as seen in **Figure *36.*** . In cast AlSi10Mg alloys the distribution of the primary silicon phase has been found to vary based on cooling rate [75].

The mechanical properties of the part depend on the size and distribution of the silicon phases. The cooling rate T has the following relationship with the cell spacing λ:

$$\lambda = CT^{-n} \text{ [76]}$$

where C and n are material dependent constants. FEM simulations can be used to determine the temperature distribution and variation across the melt pool. Y.J. Liu et al studied the cooling rates from the surface to the inside of the build within a depth of 100 μm in SLM processed AlSi10Mg alloy. They evaluated a cooling rate of 1.44×10^6 K/s at the top and a cooling rate of $\leq1\times10^3$ K/s towards the inside of the build. They also reported a decrease in microhardness from the surface to the inside of the build [37]. This agrees with the observed microstructure in our LENS® sample.

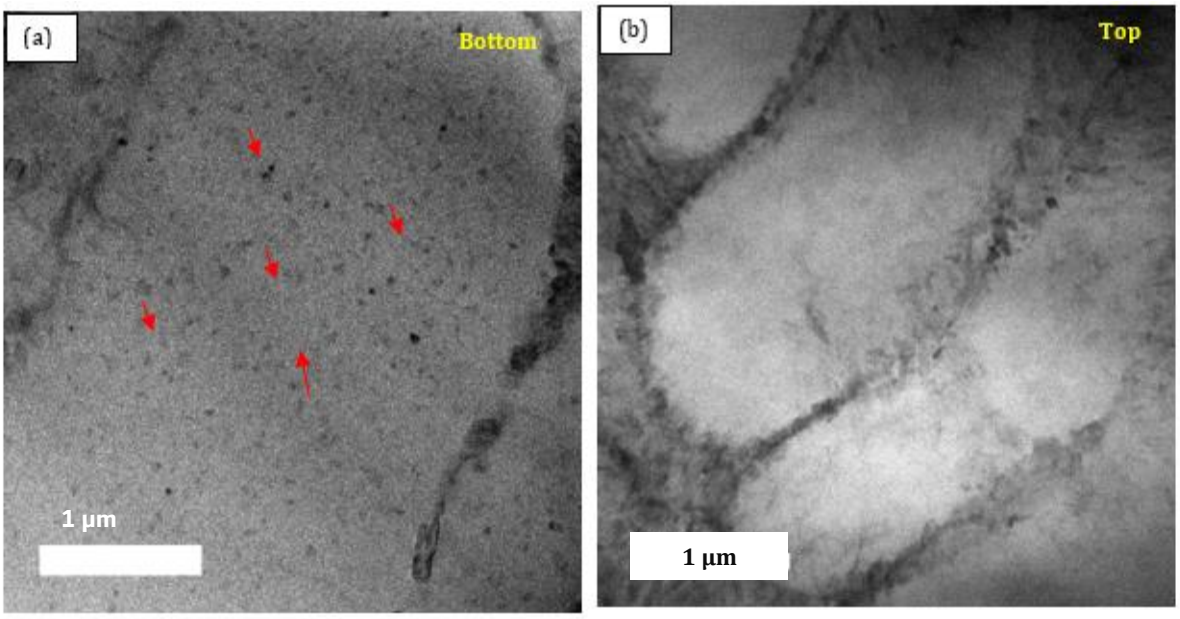

Figure 36 TEM micrographs taken from a region at the (a) bottom of the build (b) top of the LENS® build (*difference in scalebars)

3.3.3 TEM Characterization of as-deposited SLM sample

In this section the as-deposited SLM samples are characterized in TEM and a comparative study of the microstructure between the as deposited LENS ® and SLM sample is done.

Figure 37 shows the microstructure of the as-deposited SLM samples. The SLM samples have a similar cellular microstructure to the LENS® sample. The cells are approximately 500 nm in size. The cells are finer than what is observed in the LENS® samples due to the higher cooling rates in the SLM. The eutectic silicon decorates the cell boundary, and the matrix is dispersed with fine primary silicon particles. The size of these particles is approximately 100 nm. ***Figure 38*** shows the eutectic and primary Si phase in the as-deposited SLM sample.

The cell size in the SLM as-deposited samples is approximately 200-600 nm, whereas the size of the cells in the as-deposited LENS® samples is approximately 1-1.5 µm. The LENS®

process employs higher energy density compared to the SLM process. The higher energy density causes an increase in the melt pool dimensions in LENS® processing compared to SLM processing. As a new layer is built, a substantial amount of the previously deposited layers is re-melted in LENS® compared to SLM. Hence in LENS®, the extraction of the heat through the substrate becomes more difficult and gradually the temperature of the sample increases. This decreases the cooling rate and there is coarsening of Al grains and precipitates [20].

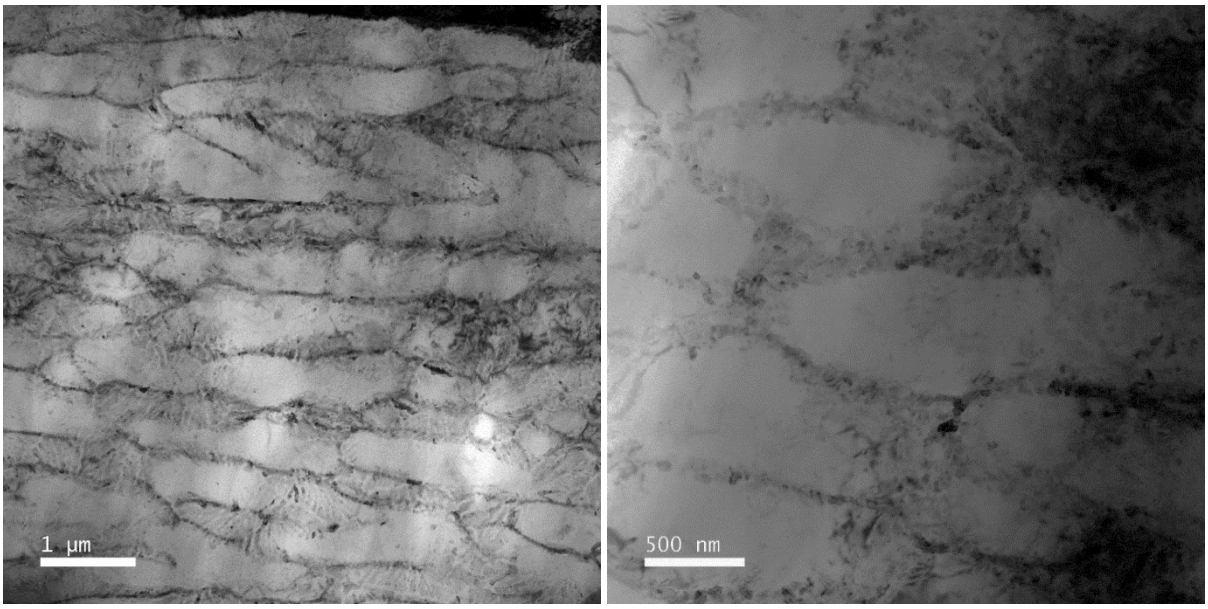

Figure 37 TEM microstructure of the as-deposited SLM sample (*difference in scalebars)

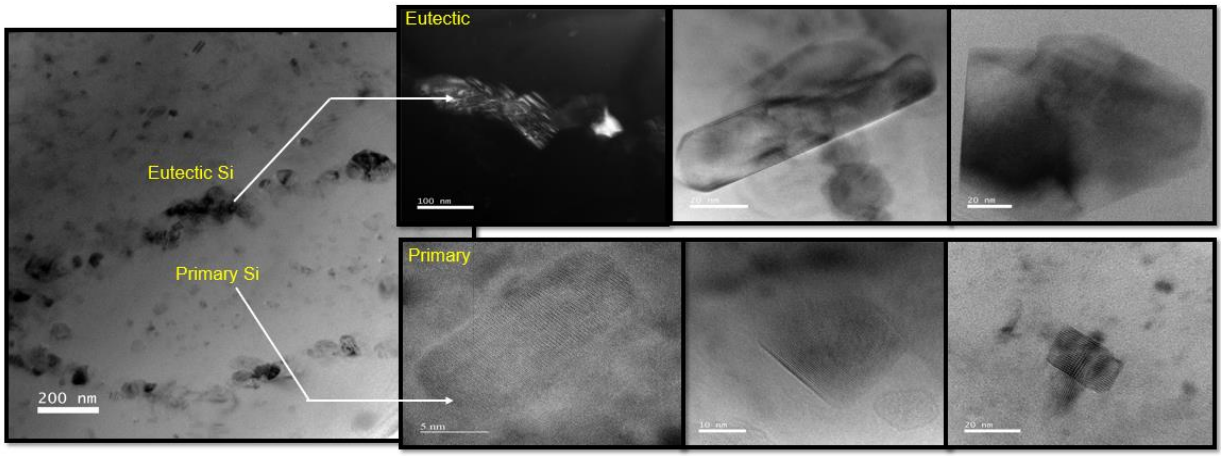

Figure 38 Eutectic and primary Si phase in the as-deposited SLM sample (difference in scalebars)

A gradient microstructure study similar to the study on the LENS® sample was performed on the SLM sample . The location of the characterized samples is seen in ***Figure 10***. ***Figure 39*** shows micrographs taken from the top and bottom of the as-deposited SLM sample. The sample from the top showed a finer microstructure compared to the cells located at the bottom. The higher cooling rates reported in the top of the build compared to the inside of the build could contribute to the finer microstructure. As the layers get built, the previous layers also get remelted and solidify. This reheating and re-melting of the layers at the bottom could also cause coarsening of the microstructure. However, the geometry of the build, in particular the height of the build can change the cooling rate across the height of the build.

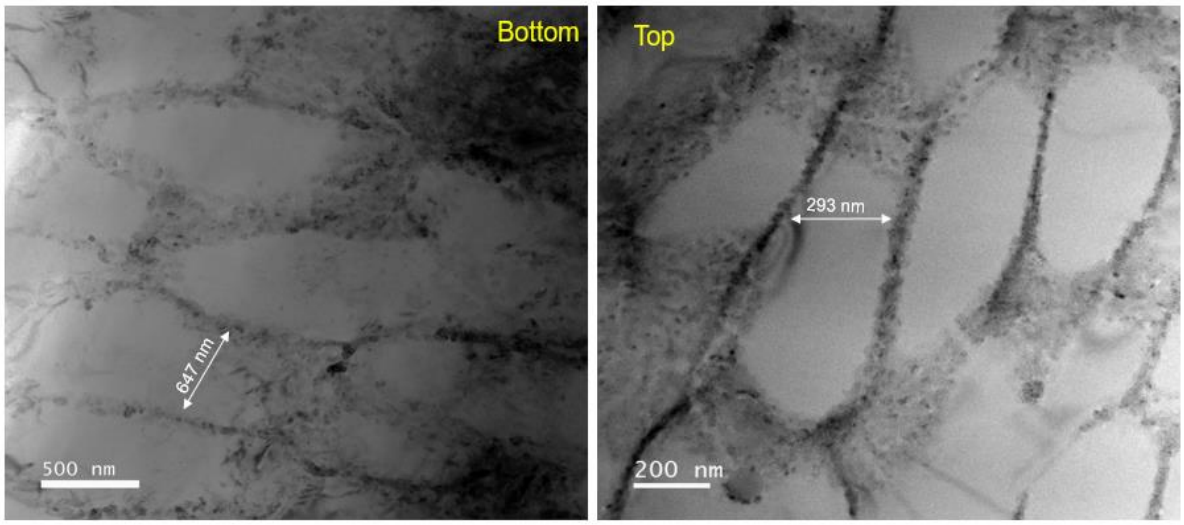

Figure 39 Gradient in microstructure across the height of the build in as-deposited SLM sample (difference in scalebars)

3.4 In-situ heating of the SLM as deposited sample

The high thermal gradients cause rapid solidification of the melt pool. As a result, grain refinement or the formation of new metastable phases is possible during the SLM process. The precipitation mechanism in SLM is complex. To understand the precipitation mechanism and the formation of the secondary phase Mg_2Si, in-situ heating in the TEM was performed.

Figure 40 shows the images of the SLM-320 sample, taken before and after heating. The sample was tilted to the <110> zone axis of aluminum. The movement of dislocations begins to occur around 90 ^{o}C, as shown by the red arrows. The continuous fibrous network of silicon begins to break down and transform into individual silicon particles. However, the precipitation of Mg_2Si was not observed. ***Figure 41*** shows the STEM-EDS characterization after heating.

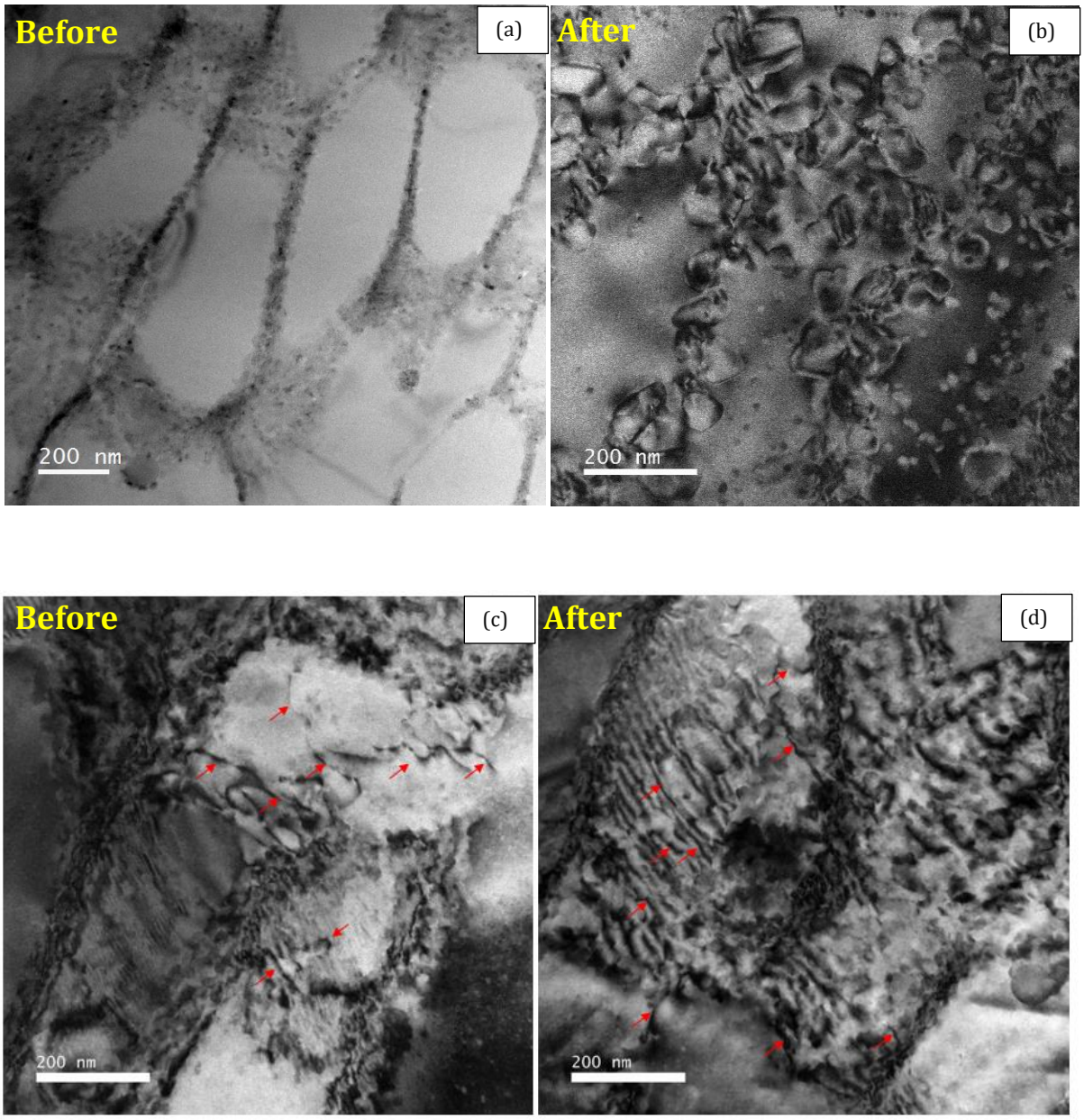

Figure 40 Before and after heating images of as-deposited SLM-320 sample. (a) & (b) Breaking of the continuous eutectic silicon phase and spherodization of Si. (b)Movement of dislocations. The red arrows highlight the movement of dislocations

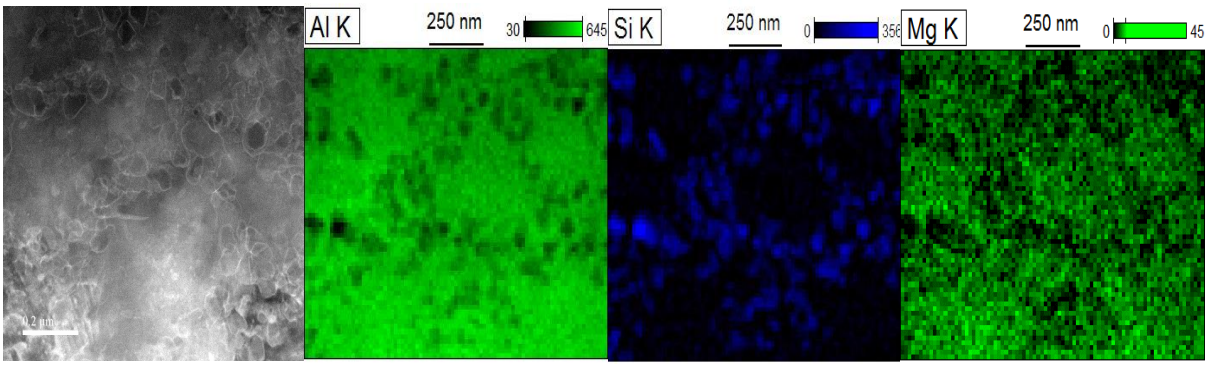

Figure 41 STEM-EDS characterization after in-situ heating

The second in-situ heating was done for a longer time to see if there is a precipitation reaction. The sample was held at 180 °C for 30 minutes. ***Figure 42*** shows the images before and after heating. The experimental results were similar to those from the previous in-situ heating. The silicon network begins to disintegrate. The disintegration of silicon occurs around 300 °C, which matches with the temperature at which the second peak was characterized in our DSC results shown in ***Figure 16***. The STEM-EDS characterization after heating, shown in ***Figure 42*** illustrates the disintegration of the Si network into individual particles and the beginning of the spherodization event.

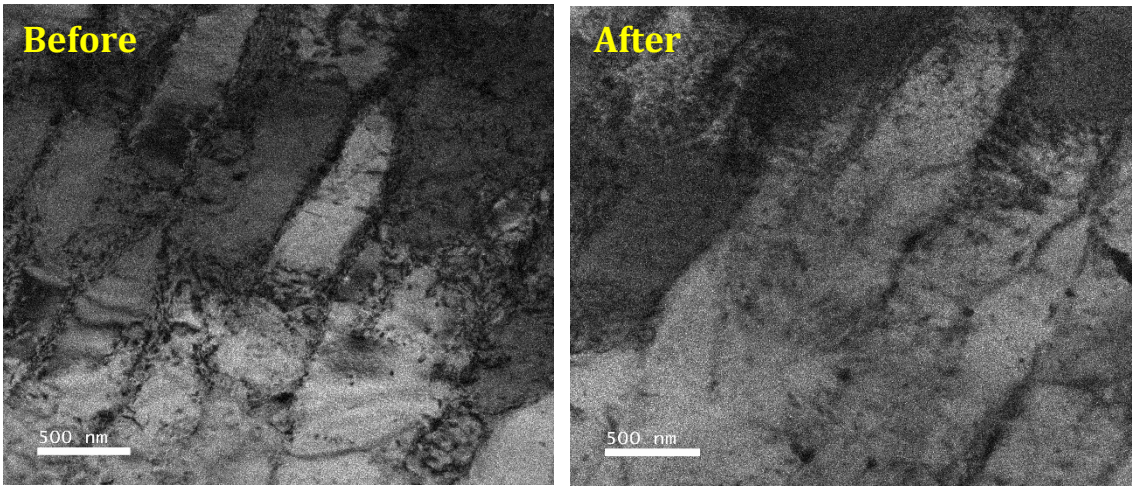

Figure 42 Before and after heating images of SLM-180 sample taken from the bottom of the build

3.5 Effect of heat treatment

The Al-Si-Mg alloys in castings have been studied for more than fifty years. The strength of these alloys can be significantly improved by heat treatment through the precipitation of the Mg_2Si phase. For cast AlSiMg alloys, T6 heat treatment has shown the best mechanical properties. A conventional T6 treatment was done on the LENS® deposited samples using two different solutionizing temperatures. The heat treatment involves taking the part to a high temperature to form a single homogenized phase. This causes the formation of a supersaturated solid solution. This step is called solution heat treatment. In the second step the solution treated part is water quenched rapidly to retain the supersaturated homogenized state. The last step, aging, is done at a temperature above room temperature to facilitate the formation of precipitates.

Figure 43 shows the XRD pattern of the as-deposited LENS® samples and the samples heat treated at different temperatures and times. The intensities of the Si peak are found to be higher in all the heat treated samples than that of the as-deposited sample. The intensity increases with the time of heat treatment. The Mg_2Si peaks also show a higher intensity in the heat treated samples.

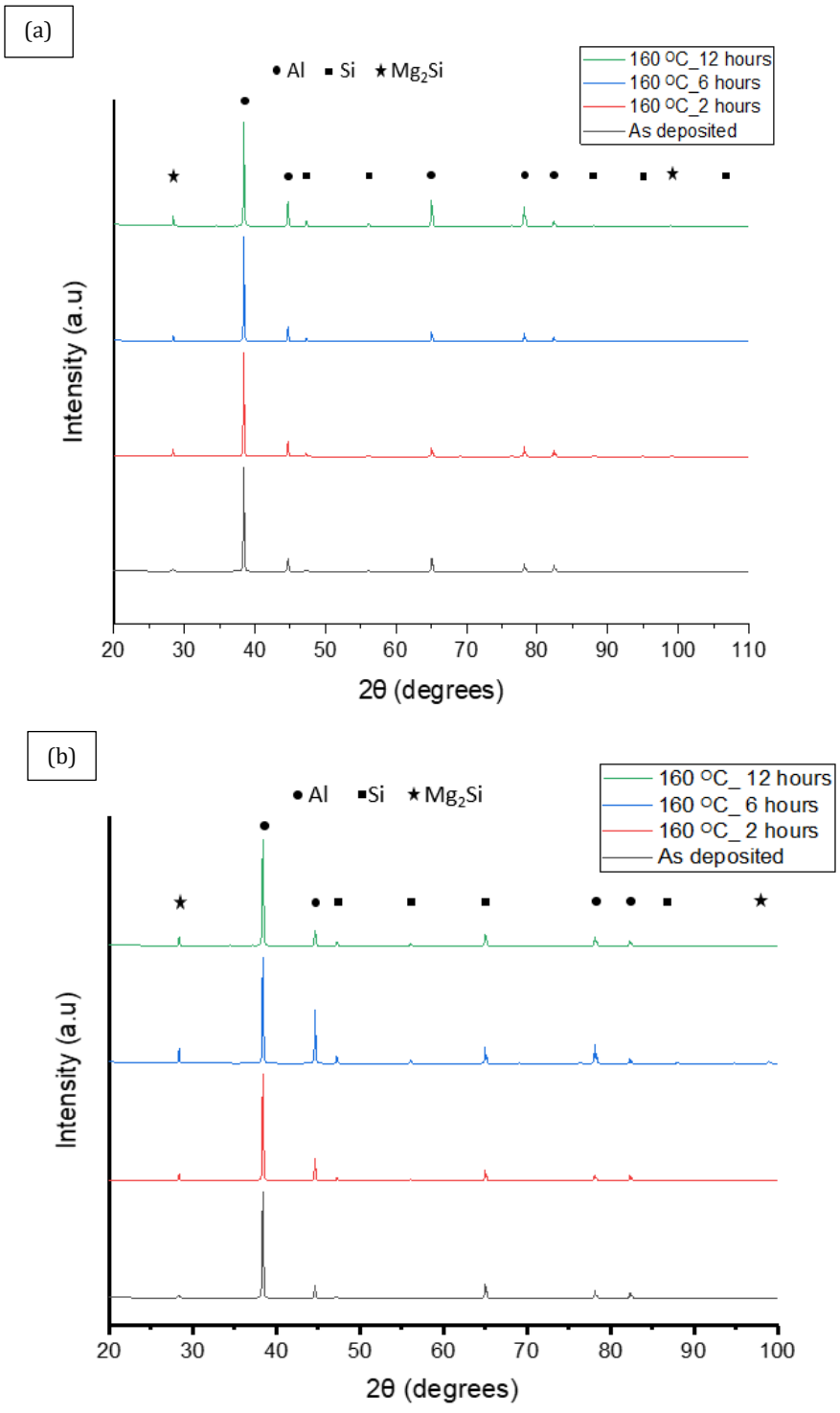

Figure 43 XRD pattern after solutionizing and artificially aging at 160 °C for various times. (a) Solutionized at 450 °C (b) Solutionized at 520 °C

The rapid cooling causes extended solubility of silicon in the aluminum matrix. Upon heat treatment, the solubility of the silicon in the matrix decreases. The silicon begins to precipitate out, which is seen as an increase in peak intensity. The precipitated silicon reacts with the magnesium to form the Mg_2Si precipitates. This increases the intensity of the Mg_2Si peaks compared to the peak intensity in the as-deposited sample. Prashanth et al., reported an increase in the crystallite size of Al from the as-deposited to the heat treated sample indicating the rejection of silicon into the matrix [77].

Figure 44 shows low magnification images of the samples solutionized at 450 ^{o}C and 520 ^{o}C, respectively. The melt pool boundaries are faintly visible in the samples solutionized at 450 ^{o}C for 2 hours, while they are no longer visible in the samples solutionized at 520^{o}C for 2 hours. The melt pool boundaries were visible in all the samples that were solutionized at 450 ^{o}C even after aging for 12 hours. The solutionizing condition has a major influence on this macro-level structure. Li et al., showed that the mechanical properties of the SLM deposited AlSi10Mg sample are dependent on the solutionizing temperature [78].

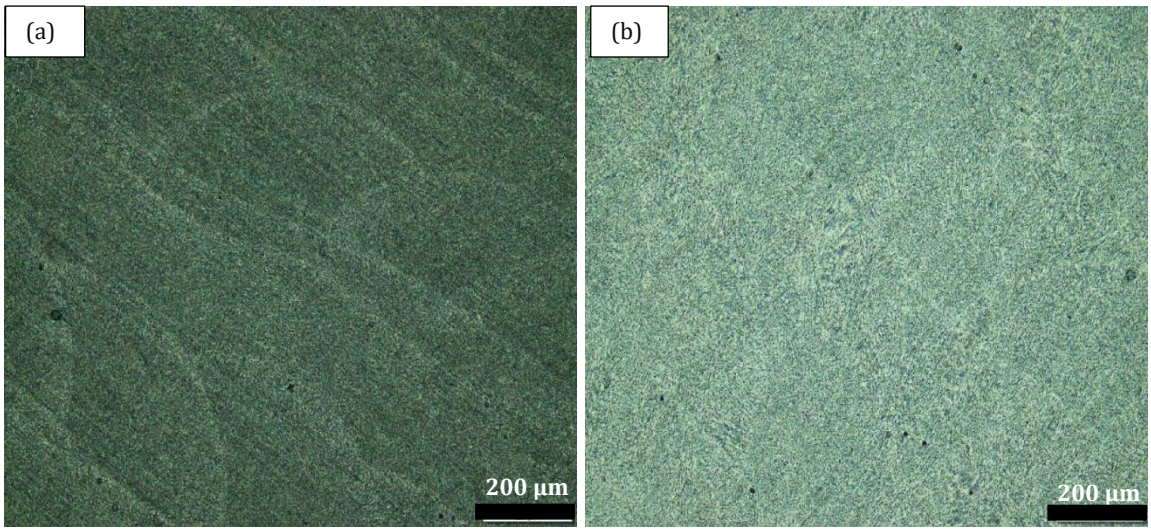

Figure 44 Low magnification images of samples: (a) solutionized at 450 ^{o}C and aged at 160 ^{o}C for 2 hours (b) solutionized at 520 ^{o}C and aged at 160 ^{o}C for 2 hours

Figure 45 and ***Figure 46*** shows the micrographs of samples solutionized at 520 °C and 450 °C, respectively, and aged for different times. There is a notable change in the morphology of the heat-treated samples. The cell structures and the eutectic fibrous silicon network are no longer visible. The silicon particles have globularized and coarsened. Globularization of silicon requires the diffusion of silicon, and it is likely that this happened during the solutionizing treatment. A common driving force for diffusion is a reduction in surface energy. At higher temperatures, enough activation energy is supplied for the diffusion to occur. The size of the silicon particles increases with the solutionizing temperature. For samples solutionized at 450°C, the silicon particle size increases from 0.8 μm to 1.3 μm. The sample solutionized at 520°C and aged for 12 hours reaches a size of 2.5-3 μm. This can be attributed to Ostwald ripening, where the larger particles grow at the expense of smaller ones to minimize energy [78].

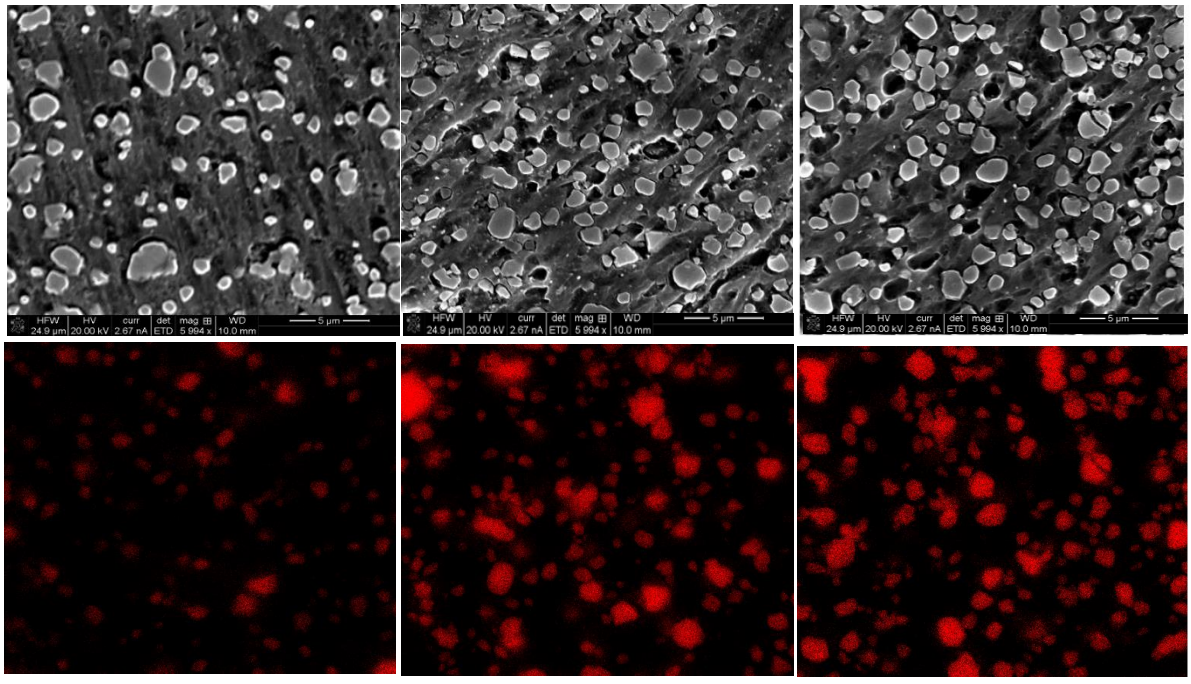

Figure 45 SEM micrographs and corresponding EDS mapping of Si of samples solutionized at 520 °C for 2 hours and aged at 160 °C for: (a) 2 hours (b) 6 hours (c) 12 hours

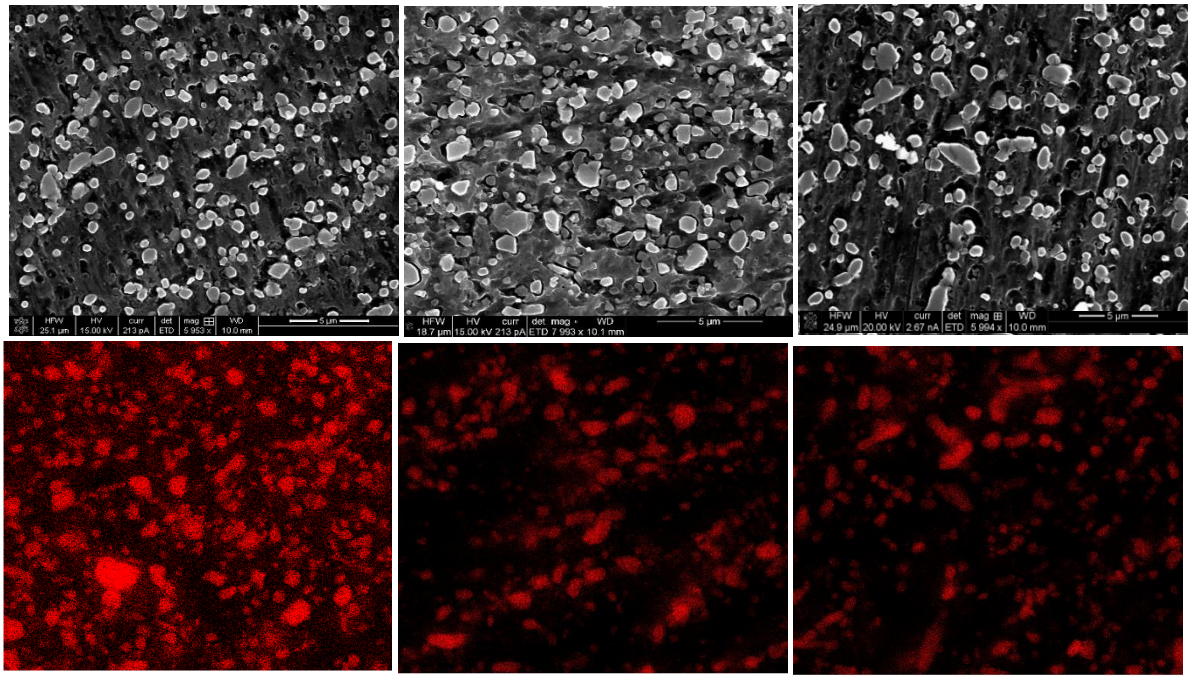

Figure 46 SEM micrographs and corresponding EDS mapping of Si of samples solutionized at 450 ^{o}C for 2 hours and aged at 160 ^{o}C for: (a) 2 hours (b) 6 hours (c) 12 hours

As the Mg_2Si precipitates were too small to be identified in the SEM even after aging, STEM-EDS characterization was done on a heat treated SLM deposited sample. The sample was solutionized at 520 ^{o}C for 2 hours and aged at 160 ^{o}C for 12 hours. ***Figure 47*** shows the EDS mapping of Al, Si and Mg taken along the <110> zone axis of Al. The cells disappear completely. The silicon particles have coarsened and spherodized. The Mg_2Si nano precipitates that were previously segregated along the cell boundaries are now precipitated at the silicon boundary. They are smaller than 500 nm. The coarsening of the Mg_2Si precipitates is not to the extent of the silicon particle coarsening. Furthermore, they are very fine compared to the size observed in castings. ***Figure 48*** shows a line scan taken across a Mg_2Si precipitate on a STEM-EDS mapping overlaying Si and Mg.

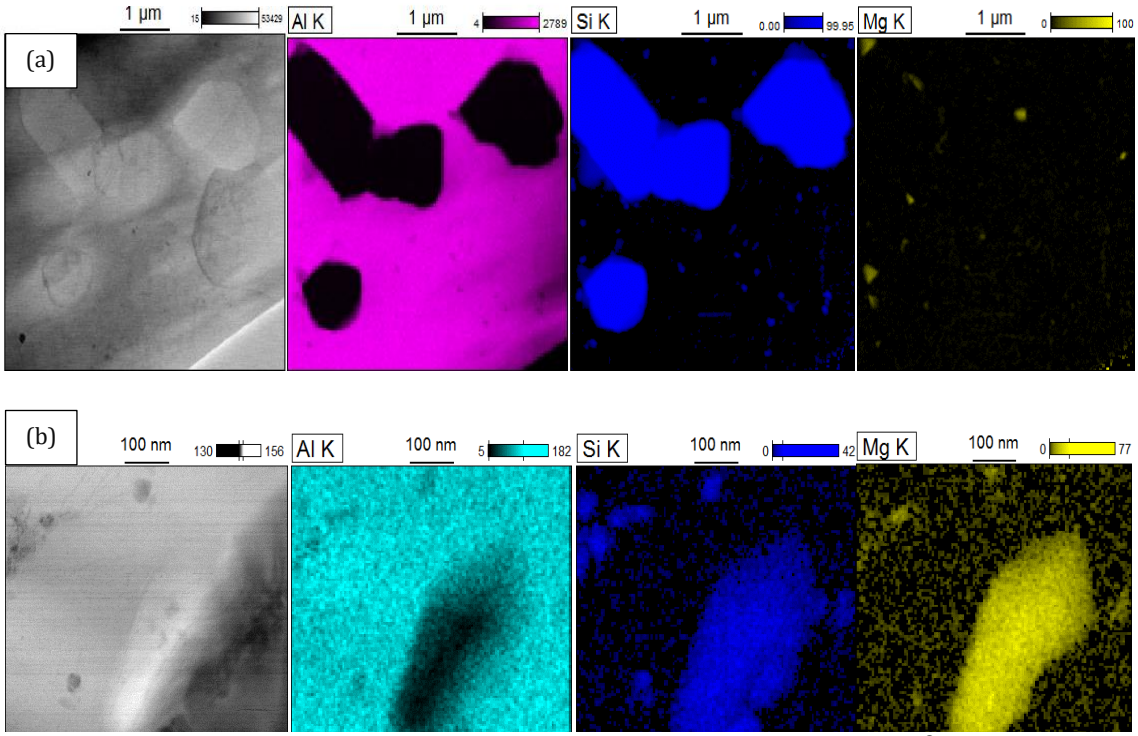

Figure 47 STEM-EDS mapping of Al, Si and Mg of a SLM sample solutionized at 520 ^{O}C for 2 hours and aged at 160 ^{O}C for 12 hours. (b) Magnified image showing the Mg_2Si precipitates

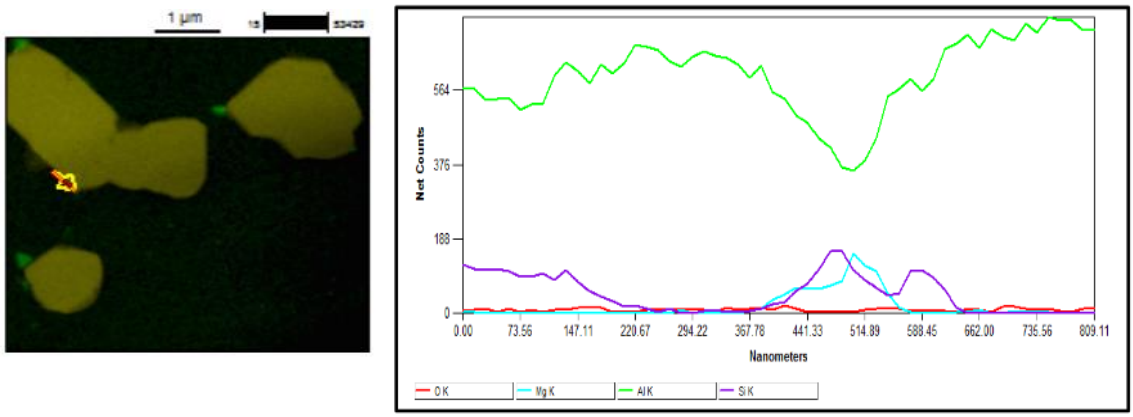

Figure 48 Line scan of the STEM-EDS image along Mg_2Si

3.6 Mechanical properties

The properties of aluminum alloys can be influenced by solidification rate, heat treatment, chemical modification and grain refining as these methods lead to microstructural changes. The mechanical properties of cast components are determined largely by the morphology, distribution and volume of Si particles in the matrix. Many studies in cast alloys have been done on this to improve the morphology of silicon [79], [80], [81]. Silicon typically has a plate-type morphology in cast materials, which decreases ductility. The morphology of the silicon particles can be changed through chemical modifiers, changing cooling rates and heat treatment. The strength and ductility of the cast parts have been found to improve considerably through heat treatments.

The mechanical properties of the AM parts, including strength, ductility and fatigue life, have been found to be equivalent to the strength of its heat treated cast counterpart [82], [83]. The high strength of the AM processed materials is mainly due to three strengthening mechanisms: (1) grain boundary strengthening, (2) solid solute strengthening, and (3) dislocation strengthening. The ultra-fine grains in AM are produced due to the high cooling rates. The grain boundaries act as pinning points for the dislocations and effectively hinder the movement and increase the yield strength.

The yield stress σ_y is related to the grain size d through the following Hall Petch relationship:

$$\sigma_y = \sigma_0 + kd^{-1/2}$$

where σ_0 is the friction stress and k is a positive constant of yielding associated with the stress required to extend dislocation activity into adjacent unyielded grains [84].

The rapid solidification causes extended solubility of the silicon in the aluminum matrix. The presence of solute in the matrix creates a tensile or compressive stress field depending on the size of the solute atoms. Dislocations are attracted to this stress field. The solute atoms diffuse to the dislocation hindering its movement and increasing the strength. The solid solute strengthening is given by the following equation [85]:

$$\Delta\tau = Gb \in \sqrt{c}$$

where $\Delta\tau$ is the difference in shear strength; G is the shear modulus; ϵ is the interaction parameter; and c is the composition.

The high density of dislocations in the material contributes to the dislocation strengthening. In heat treatable alloys, precipitation hardening is another mechanism through which the strength of the material improves. The precipitates hinder the movement of dislocations until a certain size below which the dislocations can bypass through the precipitates.

The average hardness of the as-deposited LENS® sample was found to be 105 HV, as seen in ***Figure 49***. This is higher than the reported 86 HV for T6 heat treated conventional cast and aged alloys [47].

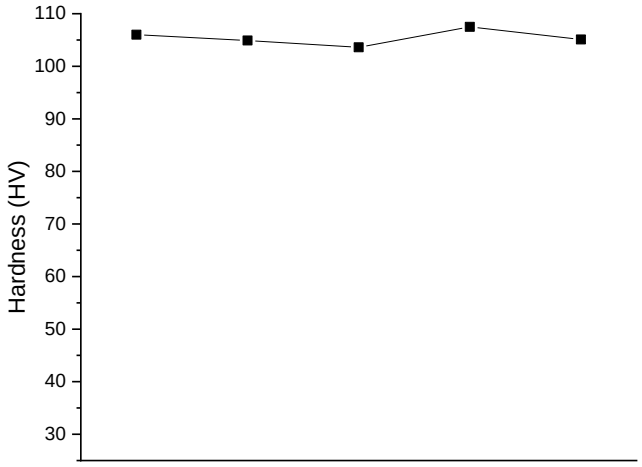

Figure 49 Vickers hardness measurement across five locations of the as-deposited LENS® sample

The mechanical properties also show a high anisotropy. Kempen et al., [47] reported that the strength of the samples built along the XY direction are higher than the strength of the samples built along the Y direction. This was because of the numerous borderline pores that form at the beginning and end of the scan vector. These pores were higher in quantity along the Z direction. However, Read at al. [82] reported that the build direction does not have a significant effect on the tensile properties.

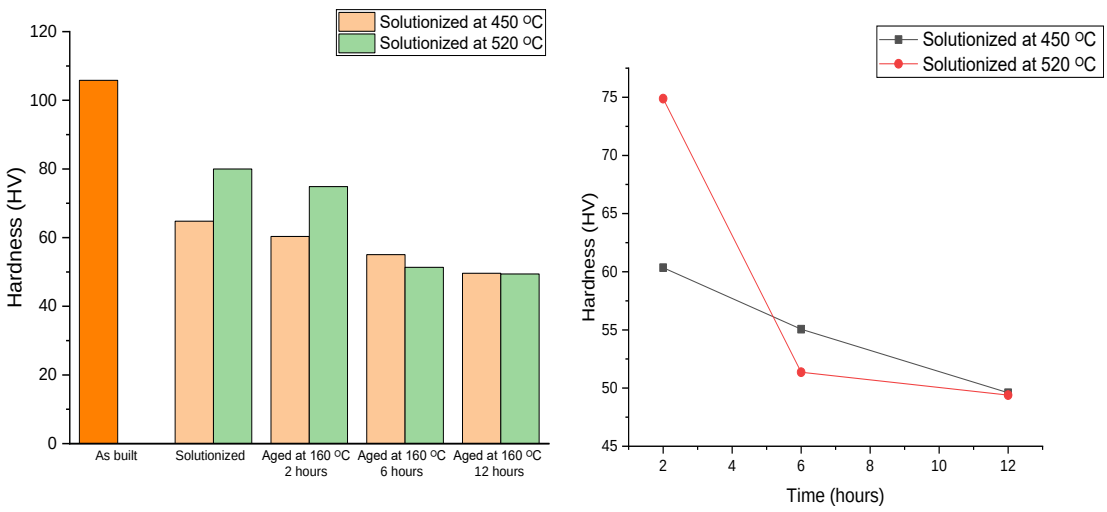

Figure 50 Hardness of the samples solutionized and aged at different temperatures and time

The hardness of the heat treated LENS® samples were studied and the results are shown in ***Figure 50***. The hardness of the heat treated samples are found to be lower than the hardness of the as-deposited samples, which is opposite to the effect found in cast alloys. The hardness of the samples decreases with increasing aging time for both the samples solutionized at 450 ^{o}C and 520 ^{o}C. This is due to the coarsening of the silicon particles and the precipitation of the silicon particles from the matrix with aging. This causes a decrease in the grain boundary strengthening and solute strengthening. The precipitation hardening of the Mg_2Si phase contributes positively to the strengthening mechanism.

Li et al., [78] reported a decrease in hardness with increasing solutionizing temperature in SLM processed AlSi10Mg samples. In our study, the hardness of the sample increases with increasing solutionizing time for similar aging conditions. The effect of heat treatment is dependent on the initial microstructures. The initial microstructure of the SLM sample is

finer than the initial microstructure of the LENS® sample. This could change the contribution from the grain boundary strengthening mechanism and result in a different response to heat treatment.

CHAPTER 4

CONCLUSIONS

In this work, microstructural evolution of AlSi10Mg alloys deposited through the LENS® and SLM techniques was studied using electron microscopy characterization techniques. The microstructure was corelated with the mechanical properties through hardness tests. The effect of heat treatment on the microstructure and hardness was also studied.

- The LENS® and the SLM deposited samples have a unique fish scale macrostructure originating from the melt pool.
- The high ratio of G:R and high cooling rates give a cellular mode of solidification for the LENS® and SLM deposited samples. The eutectic silicon is observed along the cell boundaries of the aluminum matrix. TEM and STEM-EDS characterization also revealed the presence of Mg_2Si precipitates along the cell boundaries.
- A gradient in microstructure is observed in both the LENS® and SLM deposited samples. The microstructure is finer at the top of the build compared to the bottom of the build, which is closer to the substrate. The re-heating of the previous layers as the new layers are deposited causes coarsening of the microstructure at the bottom. The heat accumulated in the bottom of the sample as the new layers are deposited also cause coarsening.
- A comparative study between the LENS® and SLM deposited sample was performed. The SLM sample has a finer microstructure compared to the LENS® sample. The

cooling rates in the LENS® process is lower in comparison to the SLM process, which results in moderate coarsening of the microstructure in the LENS® process.

- In-situ heating in TEM was conducted on the as-deposited SLM sample. The beginning of the silicon spherodization and break down of the fibrous eutectic silicon network was observed.
- The fine microstructure of the LENS® samples imparts superior hardness to the as-deposited LENS® sample. A hardness value of 105 HV was determined.
- A conventional T6 heat treatment was performed on the as-deposited LENS® samples. Upon heat treatment, the cellular network breaks down and the silicon particles begin to coarsen and reach a size of 3 μm. The Mg_2Si precipitates along the Si boundary and are very fine.
- The hardness of the heat treated samples are lower than the as-deposited sample due to the coarsening of the silicon.

Future Work:

- To study the formation and growth of the primary silicon phase in the as-deposited LENS® and SLM samples, a longer in-situ heating experiment in the TEM at higher temperatures can be performed to observe the precipitation.
- The LENS® and the SLM samples show different textures. The crystallographic orientation relationship of the Mg_2Si precipitates with the aluminum matrix and the silicon phase needs to be further studied. The precipitation sequence of the Mg_2Si phase in LENS® can be understood through further heat treatment investigations and HRTEM studies of the artificially aged samples.

- The response of the LENS® samples to heat treatment is different from the SLM samples as seen from the hardness tests. A clearer understanding of the contribution from each strengthening mechanism is required through modelling.
- The effect of heat treatment on other mechanical properties such as ductility, tensile strength and fatigue needs to be studied.

REFERENCES

[1] L. J. Smit and J. H. V. Dijk, Eds., *Powder metallurgy research trends*. New York: Nova Science Publishers, 2009.

[2] D. L. Bourell and J. J. Beaman, "A Brief History of Additive Manufacturing and the 2009 Roadmap for Additive Manufacturing: Looking Back and Looking Ahead," p. 7, 2009.

[3] S. H. Huang, P. Liu, A. Mokasdar, and L. Hou, "Additive manufacturing and its societal impact: a literature review," *Int. J. Adv. Manuf. Technol.*, vol. 67, no. 5–8, pp. 1191–1203, Jul. 2013.

[4] "F2792-WITHDRAWN.10151.pdf." .

[5] N. Guo and M. C. Leu, "Additive manufacturing: technology, applications and research needs," *Front. Mech. Eng.*, vol. 8, no. 3, pp. 215–243, Sep. 2013.

[6] "KTerrassa Masters Thesis_2017.pdf." .

[7] B. Zheng, Y. Zhou, J. E. Smugeresky, J. M. Schoenung, and E. J. Lavernia, "Thermal Behavior and Microstructural Evolution during Laser Deposition with Laser-Engineered Net Shaping: Part I. Numerical Calculations," *Metall. Mater. Trans. A*, vol. 39, no. 9, pp. 2228–2236, Sep. 2008.

[8] Z. Wang, T. A. Palmer, and A. M. Beese, "Effect of processing parameters on microstructure and tensile properties of austenitic stainless steel 304L made by directed energy deposition additive manufacturing," *Acta Mater.*, vol. 110, pp. 226–235, May 2016.

[9] "Effects of process time interval and heat treatment on the mechanical and microstructural properties of direct laser deposited 316L stainless steel - ScienceDirect." [Online]. Available: https://www.sciencedirect.com/science/article/pii/S0921509315302082. [Accessed: 15-May-2018].

[10] L. Peng *et al.*, "Direct laser fabrication of nickel alloy samples," *Int. J. Mach. Tools Manuf.*, vol. 45, no. 11, pp. 1288–1294, Sep. 2005.

[11] "Direct laser deposition of in situ Ti–6Al–4V–TiB composites - ScienceDirect." [Online]. Available: https://www.sciencedirect.com/science/article/pii/S0921509303002995. [Accessed: 15-May-2018].

[12] E. Brandl, U. Heckenberger, V. Holzinger, and D. Buchbinder, "Additive manufactured AlSi10Mg samples using Selective Laser Melting (SLM): Microstructure, high cycle fatigue, and fracture behavior," *Mater. Des.*, vol. 34, pp. 159–169, Feb. 2012.

[13] "Selective laser melting of aluminum alloys | MRS Bulletin | Cambridge Core." [Online]. Available: https://www.cambridge.org/core/journals/mrs-bulletin/article/selective-laser-melting-of-aluminum-alloys/EC1799D2905FA070C95CCAB8A91BF64D. [Accessed: 15-May-2018].

[14] D. Buchbinder, H. Schleifenbaum, S. Heidrich, W. Meiners, and J. Bültmann, "High Power Selective Laser Melting (HP SLM) of Aluminum Parts," *Phys. Procedia*, vol. 12, pp. 271–278, Jan. 2011.

[15] F. Trevisan *et al.*, "On the Selective Laser Melting (SLM) of the AlSi10Mg Alloy: Process, Microstructure, and Mechanical Properties," *Materials*, vol. 10, no. 1, Jan. 2017.
[16] R. UDROIU, "POWDER BED ADDITIVE MANUFACTURING SYSTEMS AND ITS APPLICATIONS," *Sci. Pap.*, vol. 10, no. 4, p. 9.
[17] K. G. Prashanth *et al.*, "Microstructure and mechanical properties of Al–12Si produced by selective laser melting: Effect of heat treatment," *Mater. Sci. Eng. A*, vol. 590, pp. 153–160, Jan. 2014.
[18] S. M. A. Al-Qawabah and A. I. O. Zaid, "Different Methods for Grain Refinement of Materials," vol. 7, no. 7, p. 8, 2016.
[19] D. Kotoban, A. Nazarov, and I. Shishkovsky, "Comparative Study of Selective Laser Melting and Direct Laser Metal Deposition of Ni3Al Intermetallic Alloy," *Procedia IUTAM*, vol. 23, pp. 138–146, Jan. 2017.
[20] H. Attar, S. Ehtemam-Haghighi, D. Kent, X. Wu, and M. S. Dargusch, "Comparative study of commercially pure titanium produced by laser engineered net shaping, selective laser melting and casting processes," *Mater. Sci. Eng. A*, vol. 705, pp. 385–393, Sep. 2017.
[21] D. Buchbinder, W. Meiners, K. Wissenbach, and R. Poprawe, "Selective laser melting of aluminum die-cast alloy—Correlations between process parameters, solidification conditions, and resulting mechanical properties," *J. Laser Appl.*, vol. 27, no. S2, p. S29205, Feb. 2015.
[22] E. O. Olakanmi, R. F. Cochrane, and K. W. Dalgarno, "A review on selective laser sintering/melting (SLS/SLM) of aluminium alloy powders: Processing, microstructure, and properties," *Prog. Mater. Sci.*, vol. 74, pp. 401–477, Oct. 2015.
[23] N. T. Aboulkhair, "Additive manufacture of an aluminium alloy: processing, microstructure, and mechanical properties," p. 293.
[24] N. T. Aboulkhair, N. M. Everitt, I. Ashcroft, and C. Tuck, "Reducing porosity in AlSi10Mg parts processed by selective laser melting," *Addit. Manuf.*, vol. 1–4, pp. 77–86, Oct. 2014.
[25] J. Jhabvala, E. Boillat, T. Antignac, and R. Glardon, "On the effect of scanning strategies in the selective laser melting process," *Virtual Phys. Prototyp.*, vol. 5, no. 2, pp. 99–109, Jun. 2010.
[26] E. Louvis, P. Fox, and C. J. Sutcliffe, "Selective laser melting of aluminium components," *J. Mater. Process. Technol.*, vol. 211, no. 2, pp. 275–284, Feb. 2011.
[27] "Selective laser sintering/melting (SLS/SLM) of pure Al, Al–Mg, and Al–Si powders: Effect of processing conditions and powder properties - ScienceDirect." [Online]. Available: https://www.sciencedirect.com/science/article/pii/S092401361300099X. [Accessed: 15-May-2018].
[28] D. Buchbinder, H. Schleifenbaum, S. Heidrich, W. Meiners, and J. Bültmann, "High Power Selective Laser Melting (HP SLM) of Aluminum Parts," *Phys. Procedia*, vol. 12, pp. 271–278, 2011.
[29] "2014-022-Gong.pdf." .
[30] N. T. Aboulkhair, I. Maskery, C. Tuck, I. Ashcroft, and N. M. Everitt, "On the formation of AlSi10Mg single tracks and layers in selective laser melting: Microstructure and nano-mechanical properties," *J. Mater. Process. Technol.*, vol. 230, pp. 88–98, Apr. 2016.

[31] L. N. Carter, C. Martin, P. J. Withers, and M. M. Attallah, "The influence of the laser scan strategy on grain structure and cracking behaviour in SLM powder-bed fabricated nickel superalloy," *J. Alloys Compd.*, vol. 615, pp. 338–347, Dec. 2014.
[32] L. Thijs, K. Kempen, J.-P. Kruth, and J. Van Humbeeck, "Fine-structured aluminium products with controllable texture by selective laser melting of pre-alloyed AlSi10Mg powder," *Acta Mater.*, vol. 61, no. 5, pp. 1809–1819, Mar. 2013.
[33] Y. Lu *et al.*, "Study on the microstructure, mechanical property and residual stress of SLM Inconel-718 alloy manufactured by differing island scanning strategy," *Opt. Laser Technol.*, vol. 75, pp. 197–206, Dec. 2015.
[34] B. Cheng, S. Shrestha, and K. Chou, "Stress and deformation evaluations of scanning strategy effect in selective laser melting," *Addit. Manuf.*, vol. 12, pp. 240–251, Oct. 2016.
[35] N. D. Alexopoulos and S. G. Pantelakis, "Quality evaluation of A357 cast aluminum alloy specimens subjected to different artificial aging treatment," *Mater. Des.*, vol. 25, no. 5, pp. 419–430, Aug. 2004.
[36] H. Ye, "An Overview of the Development of Al-Si-Alloy Based Material for Engine Applications," *J. Mater. Eng. Perform.*, vol. 12, no. 3, pp. 288–297, Jun. 2003.
[37] Y. J. Liu, Z. Liu, Y. Jiang, G. W. Wang, Y. Yang, and L. C. Zhang, "Gradient in microstructure and mechanical property of selective laser melted AlSi10Mg," *J. Alloys Compd.*, vol. 735, pp. 1414–1421, Feb. 2018.
[38] J. Wang, Z. Guo, J. L. Song, W. X. Hu, J. C. Li, and S. M. Xiong, "Morphology transition of the primary silicon particles in a hypereutectic A390 alloy in high pressure die casting," *Sci. Rep.*, vol. 7, no. 1, p. 14994, Nov. 2017.
[39] S. Alkahtani, E. Elgallad, M. Tash, A. Samuel, and F. Samuel, "Effect of Rare Earth Metals on the Microstructure of Al-Si Based Alloys," *Materials*, vol. 9, no. 1, p. 45, Jan. 2016.
[40] "On the Selective Laser Melting (SLM) of the AlSi10Mg Alloy: Process, Microstructure, and Mechanical Properties." [Online]. Available: https://www.ncbi.nlm.nih.gov/pmc/articles/PMC5344617/. [Accessed: 15-May-2018].
[41] M. I. Daoudi, A. Triki, and A. Redjaimia, "DSC study of the kinetic parameters of the metastable phases formation during non-isothermal annealing of an Al–Si–Mg alloy," *J. Therm. Anal. Calorim.*, vol. 104, no. 2, pp. 627–633, May 2011.
[42] W. E. Frazier, "Metal Additive Manufacturing: A Review," *J. Mater. Eng. Perform.*, vol. 23, no. 6, pp. 1917–1928, Jun. 2014.
[43] Y. Birol, "Microstructural characterization of a rapidly-solidified Al-12 wt% Si alloy," *J. Mater. Sci.*, vol. 31, no. 8, pp. 2139–2143, Jan. 1996.
[44] T. Hu, K. Ma, T. D. Topping, J. M. Schoenung, and E. J. Lavernia, "Precipitation phenomena in an ultrafine-grained Al alloy," *Acta Mater.*, vol. 61, no. 6, pp. 2163–2178, Apr. 2013.
[45] K. Ma, T. Smith, T. Hu, T. D. Topping, E. J. Lavernia, and J. M. Schoenung, "Distinct Hardening Behavior of Ultrafine-Grained Al-Zn-Mg-Cu Alloy," *Metall. Mater. Trans. A*, vol. 45, no. 11, pp. 4762–4765, Oct. 2014.
[46] E. Sjölander and S. Seifeddine, "The heat treatment of Al–Si–Cu–Mg casting alloys," *J. Mater. Process. Technol.*, vol. 210, no. 10, pp. 1249–1259, Jul. 2010.
[47] K. Kempen, L. Thijs, J. Van Humbeeck, and J.-P. Kruth, "Mechanical Properties of AlSi10Mg Produced by Selective Laser Melting," *Phys. Procedia*, vol. 39, pp. 439–446, Jan. 2012.

[48] K. Grjotheim, O. Herstad, and J. M. Toguri, “THE ALUMINUM REDUCTION OF MAGNESIUM OXIDE: I. THE VAPOR PRESSURE OF MAGNESIUM OVER THE SYSTEM Al–MgO,” *Can. J. Chem.*, vol. 39, no. 3, pp. 443–450, Mar. 1961.
[49] I. Yadroitsev, P. Krakhmalev, I. Yadroitsava, P. Bertrand, and I. Smurov, “Energy input effect on the microstructure, morphology and stability of single track from metallic powder in selective laser melting,” p. 35.
[50] J. H. Tan, W. L. E. Wong, and K. W. Dalgarno, “An overview of powder granulometry on feedstock and part performance in the selective laser melting process,” *Addit. Manuf.*, vol. 18, pp. 228–255, Dec. 2017.
[51] “Powder characterization.html.” .
[52] K. M. O’Donnell and T. B. Sercombe, “Selective laser melting of Al-12Si alloy: Enhanced densification via powder drying,” *Addit. Manuf.*, vol. 10, pp. 10–14, Apr. 2016.
[53] W. Li *et al.*, “Effect of heat treatment on AlSi10Mg alloy fabricated by selective laser melting: Microstructure evolution, mechanical properties and fracture mechanism,” *Mater. Sci. Eng. A*, vol. 663, pp. 116–125, Apr. 2016.
[54] L. P. Lam, D. Q. Zhang, Z. H. Liu, and C. K. Chua, “Phase analysis and microstructure characterisation of AlSi10Mg parts produced by Selective Laser Melting,” *Virtual Phys. Prototyp.*, vol. 10, no. 4, pp. 207–215, Oct. 2015.
[55] A. Aversa *et al.*, “Effect of Process and Post-Process Conditions on the Mechanical Properties of an A357 Alloy Produced via Laser Powder Bed Fusion,” *Metals*, vol. 7, no. 2, p. 68, Feb. 2017.
[56] J. Fiocchi, A. Tuissi, P. Bassani, and C. A. Biffi, “Low temperature annealing dedicated to AlSi10Mg selective laser melting products,” *J. Alloys Compd.*, vol. 695, pp. 3402–3409, Feb. 2017.
[57] X. Li *et al.*, “Structure and Mechanical Properties of the AlSi10Mg Alloy Samples Manufactured by Selective Laser Melting,” *IOP Conf. Ser. Mater. Sci. Eng.*, vol. 269, p. 012081, Nov. 2017.
[58] J. Smith *et al.*, “Linking process, structure, property, and performance for metal-based additive manufacturing: computational approaches with experimental support,” *Comput. Mech.*, vol. 57, no. 4, pp. 583–610, Apr. 2016.
[59] P. C. Collins, D. A. Brice, P. Samimi, I. Ghamarian, and H. L. Fraser, “Microstructural Control of Additively Manufactured Metallic Materials,” *Annu. Rev. Mater. Res.*, vol. 46, no. 1, pp. 63–91, Jul. 2016.
[60] B. Cheng, J. Lydon, K. Cooper, V. Cole, P. Northrop, and K. Chou, “Melt Pool Dimension Measurement In Selective Laser Melting Using Thermal Imaging,” p. 12.
[61] X. P. Li *et al.*, “A selective laser melting and solution heat treatment refined Al–12Si alloy with a controllable ultrafine eutectic microstructure and 25% tensile ductility,” *Acta Mater.*, vol. 95, pp. 74–82, Aug. 2015.
[62] “Morphology transition of the primary silicon particles in a hypereutectic A390 alloy in high pressure die casting | Scientific Reports.” [Online]. Available: https://www.nature.com/articles/s41598-017-15223-w. [Accessed: 16-May-2018].
[63] “ASM Alloy Phase Diagram Database™ - ASM International.” [Online]. Available: https://www.asminternational.org/materials-resources/online-databases/-/journal_content/56/10192/15469013/DATABASE. [Accessed: 19-May-2018].
[64] S. D. McDonald, K. Nogita, and A. K. Dahle, “Eutectic nucleation in Al–Si alloys,” *Acta Mater.*, vol. 52, no. 14, pp. 4273–4280, Aug. 2004.

[65] F. Wang, Z. Liu, D. Qiu, J. A. Taylor, M. A. Easton, and M.-X. Zhang, "Revisiting the role of peritectics in grain refinement of Al alloys," *Acta Mater.*, vol. 61, no. 1, pp. 360–370, Jan. 2013.
[66] T. B. Sercombe and X. Li, "Selective laser melting of aluminium and aluminium metal matrix composites: review," *Mater. Technol.*, pp. 1–9, Mar. 2016.
[67] A. M. Bastawros and M. Z. Said, "AI-12.5 wt % Si ribbons prepared by melt spinning," *J. Mater. Sci.*, vol. 28, no. 5, pp. 1143–1146, Mar. 1993.
[68] W. Li *et al.*, "Effect of heat treatment on AlSi10Mg alloy fabricated by selective laser melting: Microstructure evolution, mechanical properties and fracture mechanism," *Mater. Sci. Eng. A*, vol. 663, pp. 116–125, Mar. 2016.
[69] "Mechanical behavior of additive manufactured, powder-bed laser-fused materials - ScienceDirect." [Online]. Available: https://www.sciencedirect.com/science/article/pii/S092150931530530X. [Accessed: 16-May-2018].
[70] B. Song *et al.*, "Differences in microstructure and properties between selective laser melting and traditional manufacturing for fabrication of metal parts: A review," *Front. Mech. Eng.*, vol. 10, no. 2, pp. 111–125, Jun. 2015.
[71] K. Sindo, *Welding Metallurgy*, Second. 1987.
[72] J. A. Taylor, "Iron-Containing Intermetallic Phases in Al-Si Based Casting Alloys," *Procedia Mater. Sci.*, vol. 1, pp. 19–33, 2012.
[73] J. Lakner, "Non-Equilibrium Solubility of Iron in Aluminium," *Key Eng. Mater.*, vol. 44–45, pp. 135–146, Jan. 1991.
[74] L. Zhou, A. Mehta, E. Schulz, B. McWilliams, K. Cho, and Y. Sohn, "Microstructure, precipitates and hardness of selectively laser melted AlSi10Mg alloy before and after heat treatment," *Mater. Charact.*, Apr. 2018.
[75] S. Wang, R. Ma, Y. Wang, Y. Wang, and L. Yang, "Growth mechanism of primary silicon in cast hypoeutectic Al-Si alloys," *Trans. Nonferrous Met. Soc. China*, vol. 22, no. 6, pp. 1264–1269, Jun. 2012.
[76] A. F. Ferreira, J. A. de Castro, and L. de O. Ferreira, "Predicting Secondary-Dendrite Arm Spacing of the Al-4.5wt%Cu Alloy During Unidirectional Solidification," *Mater. Res.*, vol. 20, no. 1, pp. 68–75, Nov. 2016.
[77] K. G. Prashanth *et al.*, "Microstructure and mechanical properties of Al–12Si produced by selective laser melting: Effect of heat treatment," *Mater. Sci. Eng. A*, vol. 590, pp. 153–160, Jan. 2014.
[78] W. Li *et al.*, "Effect of heat treatment on AlSi10Mg alloy fabricated by selective laser melting: Microstructure evolution, mechanical properties and fracture mechanism," *Mater. Sci. Eng. A*, vol. 663, pp. 116–125, Apr. 2016.
[79] M. Timpel *et al.*, "The role of strontium in modifying aluminium–silicon alloys," *Acta Mater.*, vol. 60, no. 9, pp. 3920–3928, May 2012.
[80] M. A. Suarez, I. Figueroa, A. Cruz, A. Hernandez, and J. F. Chavez, "Study of the Al-Si-X system by different cooling rates and heat treatment," *Mater. Res.*, vol. 15, no. 5, pp. 763–769, Oct. 2012.
[81] L. Kuchariková, E. Tillová, and M. Chalupová, "The Si Particles Morphology in Hypoeutectic Al-Si Casts," *Mater. Today Proc.*, vol. 3, no. 4, pp. 1031–1036, Jan. 2016.

[82] N. Read, W. Wang, K. Essa, and M. M. Attallah, “Selective laser melting of AlSi10Mg alloy: Process optimisation and mechanical properties development,” *Mater. Des. 1980-2015*, vol. 65, pp. 417–424, Jan. 2015.
[83] N. E. Uzan, R. Shneck, O. Yeheskel, and N. Frage, “Fatigue of AlSi10Mg specimens fabricated by additive manufacturing selective laser melting (AM-SLM),” *Mater. Sci. Eng. A*, vol. 704, pp. 229–237, Sep. 2017.
[84] E. O. Hall, “The Deformation and Ageing of Mild Steel: III Discussion of Results,” *Proc. Phys. Soc. Sect. B*, vol. 64, no. 9, p. 747, 1951.
[85] Ø. Ryen, B. Holmedal, O. Nijs, E. Nes, E. Sjölander, and H.-E. Ekström, “Strengthening mechanisms in solid solution aluminum alloys,” *Metall. Mater. Trans. A*, vol. 37, no. 6, pp. 1999–2006, Jun. 2006.